

# Experimental study of different materials in fluidized beds with a beam-down solar reflector for CSP applications.

M. Díaz-Heras<sup>a,\*</sup>, C. Barreneche<sup>b</sup>, J.F. Belmonte<sup>a,c</sup>, A. Calderón<sup>b</sup>, A.I. Fernández<sup>b</sup>, J.A. Almendros-Ibáñez<sup>a,c</sup>

<sup>a</sup>*Renewable Energy Research Institute, Section of Solar and Energy Efficiency, C/ de la Investigación s/n, 02071, Albacete, Spain*

<sup>b</sup>*Department of Materials Science & Physical Chemistry, Universitat de Barcelona, Martí i Franqués 1, 28028, Barcelona, Spain*

<sup>c</sup>*Escuela de Ingenieros Industriales, Dpto. de Mecánica Aplicada e Ingeniería de Proyectos, Castilla-La Mancha University, Campus universitario s/n, 02071, Albacete, Spain*

---

## Abstract

Fluidized beds are particularly suitable for integration into Concentrated Solar Power (CSP) plants with beam-down reflectors. Due to the high mixing rates and heat diffusion typical of fluidized beds, they enable the highly concentrated solar flux from the beam-down reflector to impinge directly on the particles. Depending on size, density, surface roughness, optical and mechanical properties, some granular materials are more appropriate than others to store thermal energy at high-temperatures in a fluidized bed. In this line, this work compares the experimental performance of three different granular materials: sand, carbo Accucast ID50 and SiC, considering different airflow rates, and two fluidization technologies: bubbling and spouted bed. Experimental tests were carried out in a facility specifically tailored for these type of tests that permitted different flow arrangements to apply different fluidization techniques using air as the working fluid, including a

---

\*Corresponding author. Tel.: +34 967599200-ext:96253  
Email address: [minerva.diaz@uclm.es](mailto:minerva.diaz@uclm.es) (M. Díaz-Heras)

beam-down reflector with a  $4kW_e$  lamp to simulate the concentrated solar radiation (peak radiation flux of  $115kW/m^2$ ).

The temperature evolution and storage/recovery efficiencies for the different materials were compared using the two fluidization technologies, and varying the radiation level and airflow rate. Because of these tests, the influence of the airflow rate and radiation levels on the thermal efficiency of the beds was evaluated. The experimental results showed that SiC was the best candidate, as it exhibited the best thermal performance, reaching a peak storage efficiency of  $\eta_C = 0.95$ , obtained with an airflow rate of  $2.5U_{mf}$ . Maximum temperatures of  $250^\circ C$  were reached in a cylindrical bed with an aspect ratio of  $L/D \approx 1$ .

*Keywords:* Thermal Energy Storage, Fluidized beds, Solar radiation on particles, CSP

---

1

## 2 1. Introduction

3 Some authors (Bandyopadhyay, 2019) claim our society is approaching  
4 a paradigm shift that will force us to entirely change our energy model. In  
5 essence, the key features of this new energy model can be grouped into three  
6 main areas of interest: improvements in energy efficiency, expansion of re-  
7 newable energies with widespread implementation of performance monitor-  
8 ing and control of energy systems based on smart data analysis. This work  
9 can be included in the first two areas since it proposes improvements in the  
10 efficiency of current Concentrated Solar Power (CSP) systems, by increasing  
11 the utilizability of solar energy and the thermodynamic efficiency of power  
12 generation systems, they may be activated by a higher temperature level.

13 In this sense, the report presented by the European Solar Thermal Electric-  
14 ity Association (Teske et al., 2016) stated that solar thermal power systems  
15 could supply as much as 6 % of global electricity demand in 2030, and this  
16 figure could easily reach 12 % in 2050. These estimates could be even higher  
17 with improvements in current solar thermal power systems. This work is  
18 mainly focused on enhancing the thermal efficiency of the power generation  
19 systems of CSP plants, which is substantially limited by the maximum op-  
20 erating temperatures that conventional Heat Transfer Fluids (HTFs) can  
21 withstand without degradation. Most common HTFs consist of thermal oils  
22 and molten salts, which cannot operate at temperatures above 400°C (Vig-  
23 narooban et al., 2015) and 565°C (Ho and Iverson, 2014; Kuravi et al., 2013),  
24 respectively. At higher temperatures, these fluids begin to degrade (thermal  
25 instability), and different components and equipment in CSP plants may  
26 be subject to severe oxidation and corrosion problems. Obviously, these  
27 maximum operating temperatures impose an important limitation on the  
28 thermodynamic efficiency of CSP systems.

29 The use of solid particles as heat transfer medium enables a significant  
30 increase in the maximum operating temperatures of CSP systems. Sev-  
31 eral studies have reported that temperatures up to 1000°C (Diago et al.,  
32 2018; Avila-Marin, 2011) have been reached in fluidized beds containing  
33 solid particles. Two main technologies can be distinguished for thermal en-  
34 ergy storage using granular materials: packed (or fixed) and fluidized beds.  
35 The former is typically used in low-temperature applications, such as do-  
36 mestic hot water or building heating systems, since the main advantage of  
37 packed beds is their characteristic temperature stratification, which low-  
38 ers solar collector operating temperatures (and therefore, increases collector  
39 performance), reduces auxiliary energy requirements and increases the bed

40 exergy content. Fluidized beds are particularly suitable for providing rapid  
41 heat diffusion of the concentrated beam radiation that reaches the CSP re-  
42 ceiver, because of the high heat transfer coefficients produced by the intense  
43 gas-particle interactions and the high mixing rates typical of fluidized beds  
44 (Almendros-Ibáñez et al., 2019). In fact, a number of authors have found  
45 that fluidized beds behave in a fashion similar to a well-mixed tank, i.e.,  
46 there are no significant thermal gradients in the bed, with the temperature  
47 being practically uniform across the entire bed (Izquierdo-Barrientos et al.,  
48 2013).

49 There are different works in the literature that focused on the use of  
50 solid particles in CSP plants. For example, research at NREL proposed  
51 the use of a free falling particle receiver on the top of a tower (Martinek  
52 et al., 2018; Morris et al., 2016) in combination of a fluidized bed as a heat  
53 exchanger system to interchange the energy stored in the particles to the  
54 power block (Ma and Martinek, 2017; Ma et al., 2017). Ho et al. (2016)  
55 studied an advanced falling particle receiver system, which was designed  
56 and constructed at Sandia National Laboratories. The thermal efficiency of  
57 this pilot plant, for inlet temperatures of around 440°C and average particle  
58 irradiance fluxes in the range of 110-211 kW/m<sup>2</sup>, varied from 60 to 65%.  
59 Other works proposed to concentrate the solar energy on the external surface  
60 of a tube, in which solid particle are fluidized and transported (Le Gal et al.,  
61 2019).

62 Recently, several works dealing with the combined performance of flu-  
63 idized beds and beam-down reflectors for CSP applications have been pub-  
64 lished. The first works date from the 1980s by Flamant (1982); Flamant  
65 and Olalde (1983), who corroborated the advantages of fluidized beds over  
66 packed beds for rapidly distributing a highly concentrated solar energy that

67 impinges on a small area of the top surface across the entire volume of  
68 the bed. More recently, Tregambi et al. (2016) experimentally studied the  
69 superficial temperature distribution on the top of a bed of particles under  
70 controlled bubbling conditions. The authors demonstrated how a continuous  
71 injection of a bubbling air stream in the bed was able to diminish the peak  
72 temperature on the top surface of the bed. Salatino et al. (2016) proposed  
73 the use of uneven and pulsed fluidization as an alternative to increase the  
74 heat diffusion efficiency in the bed, which helps to distribute the concen-  
75 trated solar energy on the top, using a lower airflow rate, and consequently,  
76 with lower pumping costs compared to a conventional bubbling fluidization.  
77 Briongos et al. (2018) proposed a numerical model of a bubbling fluidized  
78 bed with a beam-down reflector, which was consistent with the experimental  
79 results of Flamant (1982). In this way, there are different works, which try  
80 to validate a prototype spouted bed fluidization receiver, through different  
81 experiments using a 3.0 kWh solar simulator (Matsubara et al., 2014) and  
82 numerical computation to get the performance (Bellan et al., 2019).

83 Almendros-Ibáñez et al. (2019) reviewed the different technologies avail-  
84 able for solar thermal energy storage applications, including packed and  
85 fluidized beds. In this review, the authors highlighted the suitability of  
86 fluidized beds for distributing concentrated solar energy due to the high  
87 gas/solid mixing rates. All the previous studies, except the very early works  
88 by Flamant (1982); Flamant and Olalde (1983), focused only on numerical  
89 and theoretical models. Tregambi et al. (2016) presents experimental data,  
90 but they studied the influence of artificially injected bubbles, rather than  
91 a real bubbling fluidized bed and for only one type of material: SiC. This  
92 work presents a comparative analysis of the behaviour of three different ma-  
93 terials (Sand, SiC and Carbo), which have suitable properties to be used in

94 a fluidized bed with concentration solar energy on the top. The properties  
95 of these materials were previously tested in a different work (Barreneche  
96 et al., Submitted for publication) by the authors, and tested that the three  
97 materials maintained their structure and properties after aging treatments  
98 up to 900 °C and being fluidized more than 250 hours. Thus, they are suit-  
99 able to be used for CSP and fluidization applications. In this work, we  
100 experimentally compared the performance of the three materials under sim-  
101 ilar fluidization and concentrated solar energy conditions. The experimental  
102 study covers two different fluidization technologies: bubbling and spouted  
103 bed, with the aim of compare both of them in terms of solar energy storage  
104 and fluidizing pumping cost. For both fluidization technologies, we per-  
105 formed an in deep analysis of temperature evolution and efficiencies for the  
106 three materials varying the airflow rate and the radiation level.

107 In the following sections, the experimental facility and materials are  
108 described in detail. Subsequently, the experimental results are presented  
109 and discussed, and the main conclusions of the work are summarized in the  
110 final section.

## 111 **2. Experimental facility and materials**

112 In this work, charging and discharging experiments were carried out,  
113 using three different granular materials fluidized under two different flu-  
114 idization techniques and varying the supply airflow rate. Figures 1(a) and  
115 1(b) show a scheme and a photo of the experimental facility, which permits  
116 the implementation of two distinct airflow configurations to provide different  
117 fluidization patterns: bubbling and spouted fluidized beds (see Figure 2).  
118 Except for the bed configuration (bubbling or spouted bed), the rest of the

119 elements in the facility are common for the different fluidization tests. In a  
120 bubbling bed, the air is uniformly distributed through the bottom section  
121 of the bed (from the distributor plate), where the turbulent motion and col-  
122 lapse of bubbles provoke a high gas/particles mixing rate (see Figure 3(a)).  
123 In contrast, in a spouted bed, the air is introduced through a small orifice at  
124 the bottom of a conical bed, creating a high-velocity vertical stream in the  
125 central region of the bed, where the particles are rapidly conveyed to the top  
126 part, being projected in the form of a fountain, according to Figure 3(b).  
127 This fluidization technology presents similar features to the uneven fluidiza-  
128 tion proposed by Salatino et al. (2016), likewise generating enhanced heat  
129 diffusion in the uneven fluidization of the incident solar energy that reaches  
130 the top surface of the bed. The geometry of the bed used in both bubbling  
131 and spouted tests, was carefully designed to minimize the loss of particles  
132 without reducing the incident radiation. In addition, the air velocity range  
133 is much lower than the terminal velocity of the particles, thus the loss of  
134 particles can be considered a minor problem.

135 The airflow required to fluidize the bed of particles is supplied by a CE-  
136 VIK PRO compressor with an operating pressure of 10 bar, and a maximum  
137 airflow rate of  $550 \frac{l}{min}$ . The airflow rate introduced in the bed is controlled  
138 by a mass flow controller, maintaining a constant inlet airflow rate. The  
139 incident radiation flux from the lamp was the only energy input in the bed.

140 [Figure 1 about here.]

141 The bubbling bed consists of a cylindrical 304 stainless steel tube, with  
142 an inner diameter of 7.62 cm and a height of 8 cm. The airflow is uniformly  
143 supplied into the bed through a distribution plate (Figure 2(a)) with a thick-  
144 ness of 1 mm and containing 44 perforations, each with a diameter of 1 mm  
145 (representing an open area of 0.8 % of the total area). The distributor plate  
146 was designed to ensure a minimum pressure drop equal to 30 % of the total  
147 bed pressure drop, a threshold value recommended by Kunii and Levenspiel  
148 (2013) for achieving a homogenous air distribution at any cross section of  
149 the bed.

150 On the other hand, the spouted bed consists of a conical 304 stainless  
151 steel bed, with a minimum inner diameter of 2 cm (air inlet at the bottom  
152 part), and a maximum inner diameter of 7.62 cm at the height of 8 cm  
153 (upper part). In this bed configuration, the air enters at the bottom of the  
154 bed conveying the particles through the central region of the bed, which  
155 are finally expelled in a fountain fashion from the center of the bed to the  
156 annular region where they fall (Figure 2(b)). In any of the bed configura-  
157 tions (spouted or bubbling bed), the upper part of the bed is open to the  
158 atmosphere.

159 The performance of the bubbling bed is monitored by a pressure sensor  
160 and 4 type T thermocouples, one of which is located in the plenum and the  
161 rest at different heights along the bed: 60 (TI-1), 40 (TI-2) and 20 mm (TI-  
162 3) measured from the distributor plate, according to Figure 1(a). Pressure is  
163 measured in the plenum of the bed by the pressure sensor. For the spouted  
164 bed, two type T thermocouples evenly distributed along the height of the  
165 bed measure the vertical temperature profile of the bed. For both cases,  
166 the temperature and pressure sensors are connected to a data acquisition  
167 system for monitoring and recording the experimental data.

168

[Figure 2 about here.]

169

[Figure 3 about here.]

170 Figures 1 and 2 show a beam-down reflector system, which includes a  
171 4 kW<sub>e</sub> Xe-lamp to simulate the effect of the incoming concentrated solar  
172 radiation in a CSP plant (solar radiation from the field of heliostats). The  
173 lamp can be regulated to provide a power of 2 or 4 kW<sub>e</sub>. The beam-  
174 down reflector system is similar to the facility proposed by Tregambi et al.  
175 (2016). An elliptical reflector was utilized in combination with the Xe-lamp  
176 to concentrate the radiation into a single point (or a very small area) of  
177 the top surface of the bed. The Xe-lamp was placed in one focus of the  
178 ellipse and the top surface of the bed of particles in the other focus, in close  
179 proximity to the most superficial temperature sensor (TI-1, in Figure 1(a))  
180 to measure the maximum temperatures. In any case, the total focal length  
181 ( $L_{focal}$ ) between the focuses was 1.29 m.

182 The radiation flux is provided by a 4kW<sub>e</sub> Xenon lamp (OSRAM XBO  
183 4000 W/HS XL OFR), similar to the one used by Tregambi et al. (2016).  
184 The experimental setup allows the power of the lamp to be regulated to  
185 supply 2 or 4 kW. Figure 4 shows the radiation distribution maps for  
186 both cases (2 and 4 kW<sub>e</sub>) measured during the calibration processes using  
187 a water-cooled radiative heat flux sensor (Vatell TG-9000). The red line  
188 represents the radiation profile for a constant power of 4 kW<sub>e</sub> along a plane  
189 corresponding to the top surface of the bed, which includes the bed diameter.  
190 The blue line shows the radiation profile for a constant power of 2 kW<sub>e</sub>.  
191 The data represented as points were obtained as the mean value of three  
192 repeated measurements. There were almost no differences between repeated  
193 measurements. As expected, the peak radiation flux occurs at the center of

194 the bed; around the peak point, the curve is gradually depressed but not  
195 truncated, exhibiting a bell-shape curve. For an electrical power of  $2\text{kW}_e$   
196 a maximum radiation flux of  $65\text{kW}/\text{m}^2$  is obtained. For the test where  
197 the lamp delivered a power of  $4\text{kW}_e$ , the peak flux was almost doubled to  
198  $115\text{kW}/\text{m}^2$ . Integrating the radiation flux profile over the top cross sectional  
199 area of the bed, the average incident radiation power on the top of the bed  
200 was  $140.63\text{ W}$  for  $2\text{kW}_e$  and  $231.32\text{ W}$  for  $4\text{kW}_e$ .

201 An overall efficiency of about  $7\%$  is obtained (defined as the ratio of the  
202 incident radiation on the top surface of the bed to the total electrical power  
203 of the lamp), which is similar to the efficiency values reported by Ma et al.  
204 (2019).

205 [Figure 4 about here.]

206 Three materials were tested in the experiments: sand, carbo and sili-  
207 con carbide (SiC). These materials were characterized in a previous work  
208 (Barreneche et al., Submitted for publication), where, in addition to their  
209 thermal and optical properties being experimentally measured (see Table 1),  
210 they were intensively tested during different aging and long-period fluidiza-  
211 tion processes to corroborate their ability to withstand the severe conditions  
212 (abrasion, erosion, extremely high temperatures, etc.) that occur within flu-  
213 idized beds in CSP systems. Table 1 summarizes the main properties of the  
214 granular materials tested, including: density ( $\rho$ ), specific heat ( $c_p$ ),  $d_{90}$  pa-  
215 rameter (which is an indicator of the size of the particles, corresponding to  
216 the diameter of  $90\%$  of sample volume), solar absorptivity and their cost per  
217 kilogram. These three particular granular materials were selected because  
218 they fulfil certain critical requirements that make them good candidates,  
219 showing a good suitability for being fluidized and simultaneously subjected

220 to extremely high solar radiation fluxes (and therefore, temperatures). For  
221 example, sand is an abundant and economical material that shows a stable  
222 behavior (i.e., without changes in its composition) after a large number of  
223 cycles of being fluidized and heated to extremely high temperatures (Diago  
224 et al., 2018). There are significant differences between the costs of the mate-  
225 rials, the most economical selection is by far sand, as its price only represents  
226 a small portion of the Carbo and SiC prices (approximately one-fourth and  
227 one-fifth, respectively).

228 Black silicon carbide has excellent optical properties, exhibiting a high  
229 absorptivity value of 0.90, close to the maximum value reported by carbo,  
230 which has an absorptivity of 0.95 (see Table 1). This feature, together with  
231 its high hardness, chemical stability, thermal shock resistance and ability  
232 to withstand high temperatures, makes it a good candidate. Some authors  
233 (Ho (2016); Flamant and Olalde (1983) have studied the potential inte-  
234 gration of this material in solar thermal power plants systems because it  
235 can reach temperatures of 1400 °C (Avila-Marin, 2011). Finally, carbo was  
236 also chosen because it is a ceramic material that presents very high particle  
237 breakdown resistance, exhibiting at the same time a notable ability to with-  
238 stand extremely high temperatures without showing any degradation in its  
239 properties.

240 [Table 1 about here.]

241 Table 1 indicates that the sand is the material with the lowest density  
242 and the highest  $d_{90}$  parameter and specific heat, while the opposite prop-  
243 erties are exhibited by carbo. In any event, despite small discrepancies  
244 between the properties of the selected materials, the three granular materi-  
245 als fall under the Geldart B classification (Geldart, 1973). According to the  
246 Geldart classification (Geldart, 1973), Geldart B particles are appropriate  
247 for use in fluidized beds because these granular solids can be relatively easy  
248 fluidized, showing a characteristic vigorous mixing generated by the forma-  
249 tion, growth, motion and final collapse of the bubbles(Kunii and Levenspiel,  
250 2013). This continuous agitation and movement of the particles inside the  
251 fluidized bed promotes a rapid heat diffusion, with the bed having a strong  
252 tendency to behave as a well-mixed tank at a uniform temperature. Ta-  
253 ble 2 summarizes the main characteristics of the measurement instruments,  
254 including its measurement ranges and associated uncertainties.

255

[Table 2 about here.]

256 *2.1. Hydrodynamics of the fluidized bed*

257 The first step to fluidize a material is to achieve the minimum fluidization  
258 velocity ( $U_{mf}$ ) in the bed, which represents the minimum airflow rate (or  
259 velocity) that needs to be supplied in a bubbling fluidized bed to counteract  
260 the weight of the particles. According to Kathuria and Saxena (1987), the  
261 pressure drop across the bed of particles ( $\Delta P_{\text{particles}}$ ) can be obtained by  
262 subtracting the total pressure drop of the system when filled with particles  
263  $\Delta P_{\text{system} + \text{particles}}$  and the pressure drop when the bed is empty  $\Delta P_{\text{system}}$   
264 (Sánchez-Delgado et al., 2011; Izquierdo-Barrientos et al., 2013) (see Equa-  
265 tion (1)) .

$$\Delta P_{\text{particles}} = \Delta P_{\text{system} + \text{particles}} - \Delta P_{\text{system}} \quad (1)$$

266 Figure 5 shows the experimentally measured  $\Delta P_{\text{particles}}$  versus the super-  
267 ficial air velocity in the bed for the three materials. The minimum fluidiza-  
268 tion velocity of each material is obtained by the intersection of the horizontal  
269 line and the fitting line adjusted for the first points of the bed pressure drop  
270 of each material. The horizontal lines represent the pressure drop generated  
271 by the weight of the particles in the bed, which is proportional to the mass  
272 of particles. This pressure drop was calculated as follows:

$$\Delta P_{\text{mass}} = \frac{m g}{\frac{\pi}{4} D^2} \quad (2)$$

273

274 The minimum fluidization velocity obtained using the described proce-  
275 dure is then converted into an airflow rate by multiplying it by the cross sec-  
276 tional area of the bed. The application of the previously mentioned graphical  
277 method yielded 24.51, 28.27, and 30.51 l/min for sand, SiC, and carbo, re-  
278 spectively. For each case, three different excess velocities over the minimum

279 fluidization velocity ( $U_{mf}$ ) were adopted, specifically 1.5, 2.0 and 2.5 times  
280  $U_{mf}$ . In this sense, although  $U_{mf}$  is different for each material, the bubbling  
281 conditions can be considered similar and comparable with each other, which  
282 allows performance comparisons to be made as the experimental conditions  
283 can be considered equivalent.

284 [Figure 5 about here.]

285 The minimum spouting velocity ( $U_{ms}$ ) in a spouted fluid bed is defined  
286 as the spout nozzle gas velocity required to initiate spouting regardless of  
287 the fluidization state of the annular region, which can be fluidized or not  
288 (Zhong et al., 2006). The minimum spouting velocity for each material was  
289 measured following the method proposed by Mathur (1974), being subse-  
290 quently visually corroborated by detecting the threshold values that make  
291 the particles fall in a fountain fashion onto the upper surface of the bed  
292 (incipient spouting) when the airflow rate is increased. Table 3 summarizes  
293 the values for both minimum bubbling and spouting fluidization velocities  
294 obtained for the different materials, together with their associated airflow  
295 rates. For the case of the spouted beds, the data refer to the minimum  
296 diameter, i.e., at the bottom of the cone.

297 [Table 3 about here.]

298 Table 3 shows the required airflow rates for both the bubbling fluidized  
 299 and spouted beds for each material. The minimum airflow rates for achieving  
 300 bubbling fluidization  $\dot{V}_{mf}$  are around 2-3 times higher than those needed  
 301 for the spouted bed  $\dot{V}_{ms}$ . However, when these values are translated into  
 302 velocities, dividing by the air inlet section, the minimum spouting velocities  
 303  $U_{ms}$  are much higher than the minimum fluidization velocities  $U_{mf}$  (between  
 304 5 and 7 times higher).

305 Table 4 shows the data of the power needed for fluidize the particles in  
 306 each case. It was simple calculated as:

$$\dot{W} = \dot{V} \Delta p_{\text{system} + \text{particles}} \quad (3)$$

307 Note that for a fluidized bed, in contrast to a packed or fixed bed, the  
 308 pressure drop of the particle does not vary with the airflow rate, the only  
 309 increase in the pressure drop is related with  $\Delta p_{\text{system}}$ . Table 4 points out  
 310 that the power needed in bubbling beds are far greater than in spouted beds.  
 311 Considering minimum fluidization ( $U/U_{mf} = 1$ ) and minimum spouting  
 312 ( $U/U_{ms} = 1$ ) conditions, it is observed that the consumption powers of  
 313 the bubbling beds are 5-9 times higher than that of spouted beds (despite  
 314 detecting in Table 3 that  $U_{ms} \sim (5 - 7) U_{mf}$ ).

315 This table also reports some drawbacks of using carbo, which is the dens-  
 316 est material according to Table 1. The fluidization of carbo with respect to  
 317 the lightest material (sand), requires an increase in the fluidization pumping  
 318 power of 1.5 times for the bubbling bed, and 2.5-3 times for the spouted bed.

319 [Table 4 about here.]

320 *2.2. Thermal energy storage capacity*

321 The aim of this work is to compare different materials under similar  
322 operating conditions. Table 5 details the mass for the different materials  
323 and fluidization techniques. The heat storage capacity for SiC and for Carbo  
324 was 714 – 720 J/K (according to the data showed in Tables 1 and 5), while  
325 for the sand, it was 586 J/K.

326 For the spouted bed, the mass of particles was selected in such a way that  
327 guaranteed the minimum height for a proper circulation of the particles in  
328 all tests. Due to the geometrical restrictions of the bed, the mass used in the  
329 spouted bed is approximately 2 to 3 times that necessary for the spouted  
330 bed (see Table 5). At laboratory-scale level, these differences may seem  
331 insignificant (a maximum discrepancy of only 103 g between materials for  
332 the bubbling fluidized bed), but in a full-scale CSP plant context, they can  
333 generate significant integration problems due to the volume to be considered  
334 in the selection of one or another material (Ma et al. (2014) and Briongos  
335 et al. (2018)).

336 [Table 5 about here.]

337 **3. Experimental results**

338 A total of 27 tests were carried out to measure the differential perfor-  
 339 mance of the bed under the two fluidization techniques (bubbling and spout-  
 340 ing), using the three different materials, and varying the airflow rate and  
 341 radiation flux. These tests were divided into charging processes (stage of en-  
 342 ergy storage) and discharging processes (stage of heat recovery). To study  
 343 the effects of the different variables, the experimental tests were grouped  
 344 into three mains campaigns, each consisting of 9 tests. The first campaign  
 345 of experimental tests (described in the subsection 3.1) was designed to an-  
 346 alyze the airflow rate influence. The second campaign (described in the  
 347 subsection 3.2) focused on the radiation flux influence, comparing the per-  
 348 formance of the bed when the lamp emits a thermal power of 2 or 4 kW<sub>e</sub>.  
 349 Finally, the third group of experimental tests (described in subsection 3.3)  
 350 dealt with the influence of the fluidization technique utilized, carrying out  
 351 9 additional tests in the spouted bed with a lamp power of 2 kW<sub>e</sub>.

352 For each group of tests, the overall bed performance can be described by  
 353 three key performance parameters: the storage efficiency during the charging  
 354 process,  $\eta_C$ , the recovery efficiency of the discharging process,  $\eta_D$  (Elsayed  
 355 et al., 1988; Izquierdo-Barrientos et al., 2013) and the recovery efficiency  
 356 evaluated in terms of the energy recovered by the airstream during the dis-  
 357 charging process,  $\eta_{\text{air}}$ . The storage efficiency is defined as follows:

$$\eta_C = \frac{E_s}{E_{in}} = \frac{m_s c_{p,s} \int_{t=0}^t dT}{\int_{t=0}^t \dot{Q}_{rad} dt} = \frac{m_s c_{p,s} (\bar{T}(t) - \bar{T}_{t=0})}{\int_{t=0}^t \dot{Q}_{rad} dt} \quad (4)$$

358 where the numerator is the thermal energy storage capacity ( $E_s$ ), and the  
 359 denominator is the total radiation energy that effectively reaches the bed  
 360 surface during an experimental test ( $E_{in}$ ).  $E_s$  can be formulated as the

361 product of the mass of solid particles ( $m_s$ ), the specific heat of each material  
 362 ( $c_{p,s}$ ) and the temperature variation between the initial temperature ( $\bar{T}_{t=0}$ )  
 363 and a certain instant of time "t" ( $\bar{T}(t)$ ), where  $\bar{T}(t)$  is computed as the  
 364 average temperature of the different thermocouples distributed along the  
 365 bed height. The incoming energy flux that effectively reaches the top surface  
 366 of the bed were evaluated through radiation , varying the power emitted by  
 367 the Xe-lamp, as depicted in Figure 4.

368 After 2 hours of operation, the Xe-lamp is switched off, initiating the  
 369 discharging process (the energy recovery stage) for an hour, maintaining a  
 370 constant airflow rate during both processes (charging and discharging). The  
 371 efficiency of the energy recovery process can be quantified using the following  
 372 expression from (Elsayed et al., 1988; Izquierdo-Barrientos et al., 2013; Xu  
 373 et al., 2013) (Equation (5)).

$$\eta_D = \frac{E_D}{E_{s,max}} = \frac{m_s c_{p,s} (\bar{T}_{max} - \bar{T}(t))}{m_s c_{p,s} (\bar{T}_{max} - T_{amb})} = \frac{\bar{T}_{max} - \bar{T}(t)}{\bar{T}_{max} - T_{amb}} \quad (5)$$

374 In Equation 5 the numerator indicates the actual energy recovered from  
 375 the bed, which is computed using the temperature difference between the  
 376 maximum value reached at the end of the charging process and, therefore,  
 377 the beginning of the discharging process,  $\bar{T}_{max}$ , and the actual temperature  
 378 at each time "t",  $\bar{T}(t)$ . The denominator expresses the maximum energy  
 379 that can be recovered from the bed, considering the temperature difference  
 380 between the maximum temperature reached and the ambient temperature,  
 381  $T_{amb}$ . All the temperatures plotted represent the average values of the three  
 382 thermocouples located along the bed height.

383 Equation 5 also expresses the effective energy recovered by the air during  
 384 the discharging process if the bed walls were replaced by adiabatic walls  
 385 avoiding heat losses to the surroundings. In a small lab-scale facility, as

386 the one used in this work, the ratio between the bed volume and its exterior  
 387 envelope area is typically very small, in our case:  $V/A = 2.22 \times 10^{-2} \text{ m}^3/\text{m}^2$ ,  
 388 and the heat losses are important. In addition, the mass of the bed walls and  
 389 distributor ( $m_w = 1.744 \text{ kg}$ ) is greater than the mass of particles contained  
 390 in the bed (see Table 5). The specific heat of the walls is  $c_{p,w} = 502 \text{ J}/(\text{kg K})$ ,  
 391 similar to the specific heat of the materials. Thus, the energy stored in the  
 392 walls and in the distributor can not be considered negligible. In fact, other  
 393 works (Izquierdo-Barrientos et al., 2015, 2016) have pointed out that the  
 394 energy stored in a bed of sand (similar to the one used in this work) with an  
 395 internal diameter of 200 mm, may easily account for over 15-20 % of the total  
 396 energy stored in the particles. In addition, Izquierdo-Barrientos et al. (2016)  
 397 remarked that the energy stored in the walls may be particularly important  
 398 for small bed diameters. For these reasons, it is convenient to define an  
 399 efficiency ratio,  $\eta_{\text{air}}$ , that relates the energy recovered by the air during the  
 400 discharging process to the total energy stored in the bed, accounting both  
 401 particles and bed walls, i.e.:

$$\eta_{\text{air}} = \frac{E_{\text{air}}}{E_{sw,max}} = \frac{\int_{t=0}^t \dot{m}_{\text{air}} c_{p,\text{air}} (T_{\text{air,out}} - T_{\text{air,in}}) dt}{(m_s c_{p,s} + m_w c_{p,w}) (\bar{T}_{max} - T_{amb})} \quad (6)$$

402

403 In the previous equation,  $m_w$  and  $c_{p,w}$  represent the mass and specific  
 404 heat of the bed walls. In the efficiency calculations, the outlet temperature  
 405 of the air during the discharging process may be assumed equal to the mean  
 406 bed temperature ( $T_{\text{air,out}} \approx \bar{T}$ ). This assumption was corroborated by previ-  
 407 ous works Izquierdo-Barrientos et al. (2016); Díaz-Heras et al. (2019), where  
 408 authors clearly observed that the outlet air temperature closely approached  
 409 the bed temperature due to the high mixing rates typical of fluidized beds.  
 410 It can also be assumed for a fluidized bed that the temperature discrepancy

411 between the particles contained in the bed (which exhibit a uniform tem-  
412 perature) and the bed walls is sufficiently small. Izquierdo-Barrientos et al.  
413 (2016) modeled a fluidized bed taking into account the heat losses through  
414 the bed walls. They used a bed manufactured with stainless steel walls and  
415 filled with sand, similar to the bed used in this work, confirming that the  
416 temperatures of the walls and particles were very similar.

### 417 *3.1. Bubbling bed: airflow rate influence*

418 To study the influence of the airflow rate in the bubbling bed, 9 dif-  
419 ferent tests varying the airflow rate were carried out, maintaining constant  
420 the radiation flux from the Xe-lamp at 2 kW. The three materials were  
421 tested considering three excess air velocities over the minimum fluidization  
422 conditions:  $U/U_{mf} = 1.5, 2.0$  and  $2.5$  (see Table 3). Figure 6 shows the tem-  
423 perature evolutions over time for the 9 tests conducted, where temperatures  
424 curves correspond to average temperatures calculated from the thermocou-  
425 ples shown in Figure 1(a). For each airflow rate tested, the duration of  
426 the charging and discharging stages corresponds to 2 and 1 hour, respec-  
427 tively. As expected, for bubbling fluidized beds, due to the high mixing  
428 rates that occur inside the bed, no significant temperature differences were  
429 measured between the three thermocouples located along the bed height,  
430 with the three presenting approximately the same temperature (bed behaves  
431 like a well-mixed bed showing a uniform temperature throughout the bed)  
432 (Izquierdo-Barrientos et al., 2013). The temperature differences between  
433 thermocouples were below 0.2 K. During the charging processes, carbo and  
434 SiC reported the maximum temperature values, while sand reached lower  
435 temperatures due to its low absorptivity.

436 For the three tested materials, lower air velocities result in higher peak

437 temperatures during the charging processes. For this reason, the maximum  
 438 temperatures during the energy storage processes occur in all the tests at  
 439  $U = 1.5 U_{mf}$ , obtaining lower peak values when the airflow is progressively  
 440 increased for the tests at  $2 U_{mf}$  and  $2.5 U_{mf}$ , respectively. During the dis-  
 441 charging process, the opposite situation is observed, where the tests using  
 442 the higher airflow rates ( $2.5 U_{mf}$ ) exhibit the faster energy recovery pro-  
 443 cesses, associated with lower temperature profiles.

444 In the context of this work, it is considered that the steady state is  
 445 reached when the temperature variation with respect to time is below  $0.5^\circ\text{C}/\text{min}$ .  
 446 This situation occurs after 3000 seconds for all cases, although, it happens  
 447 slightly faster for the tests using higher airflows. The difference between the  
 448 transient and steady state as a function of the airflow can be well distin-  
 449 guished in the case of sand, showing that the steady state using a airflow of  
 450  $2.5 U_{mf}$  is reached approximately after 2000 seconds, only a few seconds later  
 451 for  $2 U_{mf}$ , while approximately after 3500 seconds for the case of  $1.5 U_{mf}$ .

452 Another interesting aspect to highlight from these tests is that both  
 453 the carbo and the sand exhibit approximately the same temperature re-  
 454 duction at steady state between tests when airflow is increased, that is,  
 455  $T_{2U_{mf}} - T_{2.5U_{mf}} \approx T_{1.5U_{mf}} - T_{2U_{mf}}$ . However, for the case of SiC, the tem-  
 456 perature profiles obtained for lower airflow rates revealed temperature reduc-  
 457 tions slightly higher than those obtained for higher airflow rates,  $T_{1.5U_{mf}} -$   
 458  $T_{2U_{mf}} > T_{2U_{mf}} - T_{2.5U_{mf}}$ .

459 Figure 7(a) shows the results of the efficiency of materials during the  
 460 charging process at  $2\text{kW}_e$ . The same behavior was found in all the tests: a  
 461 bell-shape evolution with a peak of efficiency at approximately 250 seconds,  
 462 and a later gradual decrease in the charging efficiency. These efficiency peaks  
 463 are due to the rapid heating of the granular material during the initial

464 periods. Although SiC and carbo have similar absorptivities (see Table  
465 1), SiC temperature rises faster, reaching more rapidly its peak charging  
466 efficiency. This faster response of SiC could be related to more favourable  
467 fluidization conditions, such as those associated with narrower particle size  
468 distributions, which facilitates a more homogeneous fluidization. At steady  
469 state, SiC and carbo achieve similar temperatures.

470 According to Equation (4), the different behaviors in  $\eta_C$  are due to the  
471 different bed temperatures during the charging, which are shown in Figure 6.  
472 From the performance curve (Figure 7(a)), it is possible to identify the peak  
473 of the SiC ( $\eta_C = 0.95$ ), and how the airflow influence on the SiC and carbo  
474 is almost negligible during the first 700 seconds of the tests. On the other  
475 hand, the sand exhibits different peak efficiencies depending on the excess  
476 air introduced in the bed ( $\eta_C = 0.47$  for the  $1.5 U_{mf}$  test and  $\eta_C = 0.53$   
477 for the  $2.5 U_{mf}$  test). At the end of the charging process, regardless of the  
478 material and airflow rate, all cases tend towards the same efficiency value  
479 (approximately  $\eta_C = 0.1$ ).

480 Figure 6 shows that the sand reaches much lower temperatures (for the  
481 same excess gas velocity) than the other two materials. These lower tem-  
482 peratures can be explained in part by the lower absorptivity of sand, also  
483 playing a role the lower energy storage capacity of the sand compared with  
484 SiC and carbo (714 – 720 vs. 586 J/K). Figure 7(a) shows that, although  
485 temperature discrepancies are apparent between carbo and sand, both ma-  
486 terials exhibit similar charging efficiencies. Assuming that the charging effi-  
487 ciency is independent of the mass of particles, the temperatures reached by  
488 a lower mass of sand (up to reach the reference energy storage capacity of  
489  $m c_p = 714 - 720 \text{ J/K}$ ) would probably approach carbo temperatures.

490 Figure 7(b) shows the discharging and air efficiencies for the three mate-

491 rials, considering the three excess airflow rates studied ( $1.5, 2$  and  $2.5U_{mf}$ ).  
492 The discharging process begins when the lamp, which emits a power of  $2\text{ kW}_e$   
493 during the previous charging stage, is turned off. In all cases,  $\eta_D$  increases  
494 with higher airflow rates, as higher air velocities promote a more vigorous  
495 bubbling, associated with higher heat transfer coefficients between the air  
496 percolating the bed and the solid particles. Similar results were reported by  
497 Izquierdo-Barrientos et al. (2013) in a fluidized bed with sand and a granu-  
498 lar PCM. The differences between  $\eta_D$  and  $\eta_{\text{air}}$  are caused by the heat losses  
499 to the surroundings, which are significant in small facilities, as the one used  
500 in this work. In general,  $\eta_{\text{air}}$  is higher for carbo, as this material requires  
501 a higher fluidization airflow rate. For tests involving a same material, the  
502 influence of the airflow rate is unclear, as increases in the airflow rate, aug-  
503 ment the energy carried by the air in form of enthalpy, but also reduce the  
504 maximum temperatures at the beginning of the discharge processes. These  
505 opposing effects might explain why higher airflow rates provoke increases in  
506  $\eta_{\text{air}}$  for sand, but decreases for SiC and carbo.

507 According to Equation 5, the discharge efficiency is estimated by the  
508 maximum temperature difference and that obtained for each instant of the  
509 test with respect to the maximum temperature difference for each test.  
510 Therefore, the greater the difference between the maximum temperature  
511 obtained and that of each instant of time, the higher is the energy release  
512 efficiency. This explains that the solid lines of the high flow tests, which had  
513 lower temperatures, are those that show the best performance.

514 [Figure 6 about here.]

515 [Figure 7 about here.]

516 *3.2. Influence of radiation power*

517 The performance of the three granular materials was evaluated vary-  
518 ing the electric power consumed by the lamp. Two radiation levels were  
519 considered: 2 and 4  $kW_e$ .

520 The different temperature profiles of sand for the three excess fluidiza-  
521 tion velocities are plotted in Figure 8(a). Temperatures of sand with 4  $kW_e$   
522 (higher temperature profiles) are perfectly distinguished from those corre-  
523 sponding to the 2  $kW_e$  tests.

524 When the lamp works at 4  $kW_e$ , the maximum temperatures in the bed  
525 decrease by approximately 20 °C for each increase in the airflow rate (from  
526  $1.5U_{mf}$  to  $2.0U_{mf}$ , and from  $2.0U_{mf}$  to  $2.5U_{mf}$ ). These temperature re-  
527 ductions were of only 10 °C for the 2  $kW_e$  cases. For the tests shown in  
528 Figure 8(a), it can be considered that the steady state is reached after ap-  
529 proximately 2000 seconds the charging process is initiated. However, for the  
530 tests with 2  $kW_e$  the transient stage is shorter, reaching faster the steady  
531 state.

532 In general, for the studied sand tests, it can be observed that doubling  
533 the radiation power causes an approximately 1.6 times increase in the max-  
534 imum temperatures. For example, for the same excess airflow ( $1.5U_{mf}$ ),  
535 the steady-state temperature obtained with 4  $kW_e$  ( $T_{4kW_e,1.5U_{mf}} = 230^\circ\text{C}$ )  
536 is 60% higher than that of 2  $kW_e$  ( $T_{2kW_e,1.5U_{mf}} = 140^\circ\text{C}$ ). This finding is  
537 related to the efficiency results shown during the charging process in Figure  
538 9(a). This figure presents the charging efficiency, and it is observed almost  
539 no differences between the curves at 2 and 4  $kW_e$ . Only a slightly increase of  
540 the maximum efficiency in the 4  $kW_e$  case, which seems to be independent  
541 of the airflow rate. The reason is that the storage capacity, relegated to the  
542 temperature differential, is compensated for by the increase in bed radia-

543 tion. In other words, the temperature ratio of the  $4\text{ kW}_e$  tests with respect  
544 to the  $2\text{ kW}_e$  tests is in the order of 1.6. This value presents exactly the same  
545 proportion as the radiated energy incident in the bed section for  $4\text{ kW}_e$  and  
546  $2\text{ kW}_e$  tests, which measured 231.32 W and 140.62 W, respectively.

547

[Figure 8 about here.]

[Figure 9 about here.]

549 Figure 8(b) shows the temperature profiles as a function of time for  
550 the different tests involving SiC. In comparison with the profiles shown for  
551 sand (Figure 8(a)), the SiC exhibits higher temperatures for both the  $2\text{ kW}_e$   
552 and  $4\text{ kW}_e$  tests. In addition, the linear relationship between steady-state  
553 temperatures and airflow rates observed for the experimental tests with sand  
554 no longer applies. Based on Figure 8(b), the same trend can be identified as  
555 in the temperature profile of the sand. Comparing the temperature profile at  
556  $2\text{ kW}_e$  of the sand and SiC, it can be identified that the range of temperature  
557 difference is somewhat greater than in sand. The charging efficiency curves  
558 for SiC are shown in Figure 9(b). In this case, only small differences can be  
559 found between the curves, indicating that the charging efficiency of SiC is  
560 nearly independent of the airflow rate and the radiation level.

561 In the case of carbo the temperature and efficiency curves are showed in  
562 Figures 8(c) and 9(c), respectively. The maximum efficiency is obtained for  
563 the maximum airflow rate ( $U = 2.5 U_{mf}$ ) and lamp power ( $4\text{ kW}_e$ ). Contrary  
564 to the other two granular materials, substantial differences are observed in  
565 the maximum charging efficiency when the incident radiation is varied. For  
566  $U \leq 2 U_{mf}$ , the maximum efficiency obtained with  $4\text{ kW}_e$  is reduced with  
567 respect to the values obtained with  $2\text{ kW}_e$ , although it increases in the case  
568 of  $U = 2.5 U_{mf}$ .

569 Regarding the discharging efficiencies, no noticeable differences between  
570 the three materials were observed when the bed is discharged from a higher  
571 temperature level (tests involving a lamp power of  $4\text{ kW}_e$ ), with the curves  
572 being similar to those plotted in Figure 7(b). Thus, to avoid duplication,  
573 these graphs have been omitted from the article.

574 *3.3. Comparison between two fluidization technology: bubbling and spouted*  
575 *beds*

576 This section addresses the differential performance of the three granular  
577 materials for the spouted bed configuration. The results obtained for the  
578 spouted bed are compared with those previously presented for the bubbling  
579 bed.

580 The two fluidization technologies are compared, applying the same radi-  
581 ation flux on the top surface of the beds (the lamp works at  $2\text{ kW}_e$ ), which  
582 requires the consideration of two significant differences between experiments:  
583 the operating airflows are different and the mass of granular material of the  
584 spouted bed is approximately half that in the bubbling bed, as shown in  
585 Tables 3 and 5.

586 Figures 10(a), 10(b) and 10(c) show the temperature evolution of sand,  
587 SiC and carbo, respectively, for the 9 tests carried out using both fluidization  
588 technologies and the different excess airflow rates when the lamp power was  
589  $2\text{ kW}_e$ . In general, the spouted bed technology has a longer warm-up period  
590 than that exhibited by the bubbling bed, that is, it presents a slower response  
591 during the initial stages of start-up. At steady state, however, the spouted  
592 beds reached higher peak temperatures. This is mainly due to aspects of the  
593 spouted bed: first, the mass of the granular solids contained in the spouted  
594 bed is approximately half that used in bubbling fluidized bed, and second,  
595 there are significant differences between the inlet airflow introduced in both  
596 fluidization technologies. Table 3 shows the minimum fluidization airflow  
597 rates for the two fluidization techniques, where it can clearly be seen that  
598 the spouted bed only requires about  $1/3$  of the minimum fluidization airflow  
599 required by the bubbling bed ( $\dot{V}_{ms} \sim 1/3 \dot{V}_{mf}$ ).

600 As in the temperature profiles obtained for the bubbling bed, the SiC

601 also reaches higher temperatures than the other two granular materials.  
602 Similarly to the bubbling bed, peak temperatures reached in the beds are  
603 higher when the airflow rate is reduced. Note that the airflow rate needed for  
604 the spouting bed is approximately half the airflow rate used in the bubbling  
605 bed. In consequence, the pumping costs are lower for the spouted bed.

606 Figure 11(a) represents the efficiency profiles as a function of time ob-  
607 tained for the sand, carbo and SiC in the spouted bed. As mentioned in  
608 the previous sections, this figure shows that the SiC performs much better  
609 than the sand or carbo. In general terms, the charging efficiency obtained  
610 using the spouted bed is lower than in the bubbling fluidized bed. For ex-  
611 ample, for the SiC case considering the same radiation flux (a lamp power of  
612  $2 \text{ kW}_e$ ), the best charging performance for the bubbling bed was  $\eta_C = 0.95$ ,  
613 while this peak for the spouted bed is less than half that value, specifically  
614  $\eta_C = 0.53$ . This behavior is directly related to the mass of particles used  
615 in each fluidization test. In short, the charging efficiency is significantly in-  
616 fluenced by the mass of particles involved. And, therefore, higher charging  
617 efficiency is obtained in the bubbling bed configuration.

618 [Figure 10 about here.]

619

[Figure 11 about here.]

620       Regarding the differential performance of the three granular materials  
621 tested, the sand shows lower efficiencies than carbo and SiC, which show  
622 overlapping and higher discharging curves. With regard to the airflow in-  
623 fluence, the highest discharging efficiencies are always observed for tests  
624 involving higher airflow rates.

625       Figure 11(b) shows the discharging efficiency obtained for each granular  
626 material when the airflow rate is varied, considering three excess minimum  
627 fluidization velocities 1.5, 2 and  $2.5 U_{mf}$ . This figure depicts the same ten-  
628 dency shown by the discharging efficiency of Figure 7(b), obtained using  
629 the bubbling fluidized bed, but exhibiting a much more curved discharg-  
630 ing efficiency, approaching 1 more slowly. This means that the discharging  
631 efficiency is lower, with it being more difficult to fully discharge the bed,  
632 since the inlet airflow rates involved are much lower than those introduced  
633 in the bubbling bed. The air efficiency is also plotted in Figure 11(b), show-  
634 ing lower values than those exhibited for the bubbling bed tests due to the  
635 lower airflow rate. In general, for a given material,  $\eta_{\text{air}}$  only varies slightly  
636 with increasing air velocities.

637       One distinguishing characteristic between both fluidization technologies  
638 is the large difference in the pumping costs needed to circulate the fluidizing  
639 air through the bed. As previously indicated (see Table 4), the airflow rate  
640 and pressure drop necessary to fully fluidize a spouted bed are typically  
641 much lower than those in a fluidized bed. For the experimental conditions  
642 of this work, the pumping power needed to maintain the particles under  
643 a continuous fluidization are between 5 and 9 times lower in the spouted  
644 bed. Figure 12 compares the ratio between the thermal energy stored in the

645 particles ( $E_s$ ), defined in Equation 4, and the total energy needed to fluidize  
 646 the particles, i.e.:

$$\frac{E_s}{W} = \frac{m_s c_{p,s} \int_{t=0}^t dT}{\int_{t=0}^t \dot{W} dt} = \frac{m_s c_{p,s} (\bar{T}(t) - \bar{T}_{t=0})}{\dot{W} t} \quad (7)$$

647 This figure clearly shows how spouted beds reach much higher values of  
 648  $E_s/W$  than bubbling beds. Although the thermal efficiency,  $\eta_C$ , is lower in  
 649 spouted beds, this is partially compensated for by the reduced values of  $W$ .  
 650 Comparing materials, in both bubbling and spouted bed, carbo presents the  
 651 lowest values due to its higher density together with the higher volumetric  
 652 flow rates required to fluidize this material. Comparing sand and SiC, the  
 653 lower density of the sand (and consequently lower pumping requirements)  
 654 compensates in part its lower thermal efficiency, and both materials exhibit  
 655 similar  $E_s/W$  ratios for the spouted bed. Regarding the bubbling bed tests,  
 656 although behaving similarly to sand, the highest values of  $E_s/W$  are reported  
 657 by SiC.

658 [Figure 12 about here.]

## 659 4. Discussion

### 660 4.1. Discussion of the results

661 According to the experimental results obtained for the three granular  
 662 materials, SiC is clearly the material that performs better in both fluidiza-  
 663 tion techniques (bubbling and spouting) when a concentrated radiation flux  
 664 impinges on the top surface of the bed. Because of its high absorptivity, this  
 665 material reaches higher temperatures during the charging process and, con-  
 666 sequently, provides the highest charging efficiency, with a peak of  $\eta_C = 0.95$

667 for  $U = 2.5 U_{mf}$ . Moreover, during the discharging process, with no inci-  
668 dent radiation on the top surface, the SiC also exhibits better efficiencies,  
669 although in this case, only small differences between the three materials are  
670 observed. The main disadvantage of SiC compared with the other materi-  
671 als, especially with sand, is its higher cost. Sand has the advantage of being  
672 abundant and cheap, particularly in regions of the planet with high levels  
673 of solar radiation throughout the year, which, in turn, are good candidate  
674 locations for installing CSP plants (Diago et al., 2018).

675 One interesting aspect observed in all experimental tests of the present  
676 work, is that the peak charging efficiency is almost independent of the in-  
677 cident radiation and airflow rate. Thus, to maximize the efficiency of the  
678 charging process of a fluidized bed for CSP applications, the fluidized bed  
679 system should be designed in such a way that the particle residence time is  
680 equal to the time needed to achieve the maximum efficiency, which for the  
681 experimental conditions of this work was approximately 250 s, regardless of  
682 the material, incident radiation level, airflow rate or fluidization technology  
683 employed.

684 Regarding the discharging process, no direct influence of the lamp power  
685 occurs, as during this stage the bed receives no incident radiation flux. The  
686 only effect is due to the initial temperature level for the discharging process  
687 (higher initial temperatures when higher radiation levels are used to charge  
688 the bed). This may justify the slightly higher efficiencies obtained with SiC,  
689 as this material reaches the highest temperatures at the end of the charging  
690 process.

691 It should be noted that in a real CSP plant with a beam-down reflec-  
692 tor, there are multiple alternatives for recovering the energy stored in the  
693 particles. It can be directly recovered from the particles themselves, or alter-

694 natively by using a heat exchanger inside the fluidized bed. See, for example  
695 the work by Fernández-Torrijos et al. (2018), who proposed the use of a plate  
696 heat exchanger for a supercritical CO<sub>2</sub> cycle. Although they proposed this  
697 system as a solution for integration into a CSP plant with free-falling par-  
698 ticles, it is perfectly applicable to a CSP system including a beam-down  
699 reflector. In any event, the heat recovery process of the energy stored in the  
700 particles in a CSP plant is highly dependent on the thermodynamic cycle in  
701 the power block.

702     One relevant characteristic observed in the three granular materials un-  
703 der fluidization conditions is the increase in the bed temperature when the  
704 airflow rate is reduced. This observation opens up the possibility of con-  
705 trolling real CSP plants with a beam-down reflector by adjusting the supply  
706 airflow rate to maintain a desired temperature within the bed, without re-  
707 quiring a complex strategy to control the concentrated radiation flux from  
708 the heliostats (Sánchez-González et al., 2017, 2018). Currently, in conven-  
709 tional CSP plants with a central receiver and molten salts as the HTF, an  
710 aiming strategy is necessary during the start-up of the plant in order not to  
711 exceed the maximum temperatures allowed, thus preventing degradation of  
712 the HTF, and other related harmful problems such as corrosion or excessive  
713 thermal stresses in the tubes. For example, during the start-up stage, when  
714 the radiation levels are low, the airflow rate can be low to permit a rapid  
715 rise in the temperature of the bed. The supply airflow rate can be gradu-  
716 ally increased as the level of beam solar radiation augments. In this sense,  
717 it should be noted that, contrary to the conventional system, in which the  
718 pressure drop is a function of the flow rate squared, the air pressure drop in  
719 a fluidized bed does not vary with higher airflow rates, and therefore, does  
720 not entail increased pumping costs. This control strategy cannot be properly

721 implemented in other systems using particles such as packed beds, indirect  
722 systems (Benoit et al., 2015; García-Triñanes et al., 2016) or free-falling  
723 particle receivers (Ho, 2016).

724       Regarding the two fluidization techniques compared in this work, bub-  
725 bling and spouted beds, it should be noted that the spouted bed presents  
726 similar results to those exhibited by the bubbling bed, but using only around  
727 one-third of the airflow rate needed for the conventional bubbling fluidized  
728 bed. This allows to pumping costs in a CSP plant to be further reduced.  
729 However, the charging efficiency is lower than in the bubbling bed case, and  
730 consequently, the time needed to fully charge the bed is longer. Neverthe-  
731 less, more developments and experiments of this type of uneven fluidization  
732 technique should be carried out in pilot plants and larger facilities (full-  
733 scale tests) to corroborate the experimental results observed in this work at  
734 lab-scale level.

735       It is interesting to notice the large differences in price between the three  
736 materials (see Table 1). Sand is by far the most economical material, with  
737 a price that depending on the actual location of the CSP plant, could even  
738 be much lower than that indicated in the table (Diago et al., 2018). In  
739 this way, it is obvious that in the design of a new CSP system including  
740 this technology, great care should be taken to ascertain if the increase in  
741 the efficiency of the system, obtained using a more costly material, such  
742 as SiC, compensates its higher price, as candidate materials compete with  
743 an abundant and inexpensive material as it is sand. A detailed economic  
744 analysis may be required to determine the best alternative.

745 *4.2. Discussion of scale-up*

746 The experimental results presented in this work were obtained in a small-  
747 scale experimental facility. Obviously, the results are not directly extrap-  
748 lable to much larger scale installations, although they certainly can spread  
749 some light about the expected behavior of a full-scale facility. Two main  
750 findings of this work can be expected: SiC will produce the best thermal  
751 performance during the charging process, and sand will be the most com-  
752 petitive material in terms of pumping costs. Additionally, in a real full-scale  
753 application, thermal losses to surroundings and wall effects will be much less  
754 important.

755 The scalability of a bubbling fluidized bed reactor has been widely stud-  
756 ied in previous works (Glicksman, 1984; Glicksman et al., 1993; Zanganeh  
757 et al., 2012). The pioneering work by Glicksman (1984) showed that to  
758 maintain a fluid-dynamics similarity when scaled-up a fluidized bed reactor,  
759 the following non-dimensional numbers should be maintained constant:

$$\frac{U \rho_g d_p}{\mu}, \quad \frac{U}{g D}, \quad \frac{\rho_g}{\rho_s}, \quad \frac{D}{H}, \quad \phi, \quad PSD \quad (8)$$

760 In order to ensure a similar bubble size distribution and bubble frequency  
761 in the scaled-up bed, the previous non-dimensional numbers have to be kept  
762 constant. The difficulty that authors found was that to strictly maintain  
763 constant all the parameters in Equation (8), it is required either use ex-  
764 tremely dense materials or beds with hugely uneven dimensions (e.g., beds  
765 with a diameter of several meters and a height of only a few centimeters)  
766 (Zanganeh et al., 2012). In addition, the non-dimensional magnitudes in  
767 Equation (8) neither account any heat transfer process nor the effects of  
768 concentrated solar energy on the top of the bed, which provoke temperature  
769 gradients between particles.

770 A similar bubble size distribution is recommended in bubbling fluidized  
771 bed reactors such as combustors and gasifiers, where the oxygen content in  
772 the air passes through the bed in the form of bubbles, reacting with the  
773 bed material (biomass or coal, for example). In small-scale facilities the  
774 bubble size can be similar to the bed size (slugging regime), whereas in  
775 full-scale installations the wall effects can be considered negligible. In our  
776 case, there are no chemical reactions, thus even bubble size distributions  
777 and frequencies are not critical aspects of the fluidization. It is important  
778 to ensure a good fluidization process throughout the cross sectional area of  
779 the bed, preventing the appearance of dead zones without being fluidized,  
780 in which particles may suffer severe overheating and sintering problems.

781 Regarding spouted beds, in addition to the non-dimensional parame-  
782 ters in Equation (8), it is also necessary to add the voidage  $\varepsilon_{mf}$ , the angle  
783 of internal friction of the particles  $\varphi$ , and the coefficient of restitution  $\varphi_p$ .  
784 These parameters are necessary due to the more frequent particle-to-particle  
785 collisions given in spouted beds as well as the greater transmission of com-  
786 pression and friction forces compared to a bubbling fluidized bed (Grace and  
787 Lim, 2011). Grace and Lim (2011) proposed as a rule of thumb for a single  
788 spouted bed, that the ratio between the bed diameter and the particle size  
789 should be:

$$\frac{D}{d_p} \leq 300 \quad (9)$$

790 For larger sizes, it is recommended the use of multiple spout geometries, in  
791 which a large cross sectional area is divided into several modular spouted  
792 beds connected in parallel. In any case, the size of each module should not  
793 exceed the limit imposed by Equation (9).

794 Another important aspect of the scale-up is the influence of the radiation

795 flux, which in this work has a maximum value around  $120 \text{ kW/m}^2$ , and in  
796 a full-scale CSP system can reach values up to  $1000 \text{ kW/m}^2$ . For example,  
797 the Miyazaki beam-down system (Kodama et al., 2014; Matsubara et al.,  
798 2015), which consisted in an elliptical reflector with 88 heliostats that cov-  
799 ered a total area of  $176 \text{ m}^2$ , reported a peak radiation flux of  $500 \text{ kW/m}^2$ ,  
800 reaching much higher temperatures than those obtained in this work. The  
801 materials used in this work were tested at higher temperatures in a different  
802 work (Barreneche et al., Submitted for publication), not exhibiting notable  
803 variations in their properties, and therefore, demonstrating they are good  
804 candidates to be used in CSP applications. Also at higher flux densities,  
805 the thermal behavior exhibited by the spouted and bubbling fluidized beds,  
806 may differ from that observed in this work, especially if multiple spouted  
807 beds arranged in parallel are used, as the benefit of the lower pumping cost  
808 of a spouted bed can be significantly reduced. At higher temperatures, the  
809 minimum fluidization velocity of the bed varies. According to some works  
810 (Guo et al., 2003; Subramani et al., 2007), the minimum fluidization velocity  
811 tends to decrease slightly with increasing temperatures. This finding can be  
812 considered advantageous since the pumping costs can be reduced.

813 In summary, for scale-up the system proposed in this work should fol-  
814 lowed different design guidelines. Initially, prior to large full-scale facilities  
815 (with  $D > 0.5 \text{ m}$ ), it is recommended the construction of a pilot small-scale  
816 facility (with  $D \sim 0.5 \text{ m}$ ) subjected to relatively high radiation flux levels  
817 (Rüdisüli et al., 2012), with the aim of evaluating the proper heat diffusion  
818 of the concentrated solar energy that impinges on the top surface of the bed.  
819 From this pilot plant, energy losses to the surroundings as well as wall effects  
820 can be also be accounted, considering that its influence will be much lower  
821 in a full-scale plant. Thus, this intermediate size will help to corroborate

822 the results obtained in this work and to define the final full-scale facility.  
823 Also, with a well designed full-scale facility is possible to perform a complete  
824 economical analysis to corroborate if the higher thermal performance of the  
825 SiC compensates its higher pumping cost, compared with other materials,  
826 such as sand.

## 827 5. Conclusions

828 The main conclusions of this work are:

- 829 1. SiC presents the highest charging and discharging efficiencies, exhibit-  
830 ing higher temperatures in the bed. The peak charging efficiency from  
831 all the conducted tests was  $\eta_C = 0.95$ , obtained for the tests using an  
832 excess airflow rate equivalent to 2.5 times the  $U_{mf}$  of the bed.
- 833 2. The three tested materials present a similar behavior: the peak tem-  
834 perature in the bed increases when the airflow rate is reduced.
- 835 3. The efficiency curves are relatively insensitive to variations in the in-  
836 cident radiation flux on the top surface of the bed. In addition, the  
837 maximum charging efficiencies for the two fluidization technologies and  
838 the three materials tested always occur at approximately 250 s.
- 839 4. Taking into account the pumping power, the thermal differences be-  
840 tween SiC and sand are reduced due to the lower density of the sand,  
841 which needs lower airflow rates and lower pumping power.
- 842 5. Spouted beds presents values of  $E_s/W$  approximately 3-5 higher than  
843 bubbling fluidized beds, due to the lower pumping requirements of  
844 spouted beds.

845 **6. Notation**

846  $c_p$  Specific heat [ $\frac{J}{kg \cdot K}$ ]

847  $D$  Bed diameter [m]

848  $d_{90}$  Particle diameter of the 90% of sample volume [m]

849  $dT$  Temperature differential [s]

850  $dt$  time differential [s]

851  $E_s$  Stored energy [J]

852  $E_{in}$  Inlet energy [J]

853  $E_D$  Recovery energy during discharging process [J]

854  $g$  gravitational constant [ $m/s^2$ ]

855  $H$  Bed height [m]

856  $m$  mass of solid particles [kg]

857  $PSD$  Particle Size Distribution [%]

858  $\dot{Q}_{rad}$  Radiation flux energy obtained by the lamp [W]

859  $T$  Temperature [K]

860  $\bar{T}(t)$  Mean temperature of different thermocouples in the bed at each  
861 instant of time [K]

862	$T_{t=0}$	Initial temperature of the test [K]
863	$T_{amb}$	Ambient temperature [K]
864	t	time [s]
865	$U$	Superficial gas velocity [m/s]
866	$U_{mf}$	Minimum fluidization velocity [m/s]
867	$U_{ms}$	Minimum spouting velocity [m/s]
868	$\dot{V}_{mf}$	Minimum fluidization airflow rate [ $m^3/s$ ]
869	$\dot{V}_{ms}$	Minimum spouting airflow rate [ $m^3/s$ ]
870	$\dot{W}$	Pumping power [W]

871 *6.1. Greek symbols*

872  $\Delta P$  Pressure drop [Pa]

873  $\eta$  Efficiency [-]

874  $\rho$  Density [ $kg/m^3$ ]

875  $\phi$  Particle sphericity [-]

876 *6.2. Subscripts*

877 C Charging process

878        *D*    Discharging process

879        *e*    Electric

880        *g*    Gas

881    max    maximum value

882        *s*    Solid particles

## 883    **7. Acknowledgments**

884        This work was partially funded by the Ministerio de Economía y Com-  
885    petitividad (Projects RTI2018-093849-B-C32 MCIU/AEI/FEDER,UE and  
886    ENE2016-78908-R) of the Spanish Government, the Regional Government of  
887    Castilla-La Mancha (project SBPLY/17/180501/000412) and the Ministerio  
888    de Ciencia, Innovación y Universidades - Agencia Estatal de Investigación  
889    (AEI) (RED2018-102431-T). The authors would like to thank the Cata-  
890    lan Government for the quality accreditation given to their research group  
891    (DIOPMA 2017 SGR 0118). DIOPMA is certified agent TECNIO in the  
892    category of technology developers from the Government of Catalonia.

## 893    **References**

894    Almendros-Ibáñez, J., Fernández-Torrijos, M., Díaz-Heras, M., Belmonte,  
895    J., Sobrino, C., 2019. A review of solar thermal energy storage in beds of  
896    particles: packed and fluidized beds. *Solar Energy* 192, 193–237.

897    Avila-Marin, A. L., 2011. Volumetric receivers in solar thermal power plants  
898    with central receiver system technology: a review. *Solar energy* 85 (5),  
899    891–910.

900 Bandyopadhyay, S., 2019. The first step towards energy revolution. *Clean*  
901 *Technologies and Environmental Policy* 21, 227–228.

902 Barreneche, C., Díaz-Heras, M., Calderón, A., M., M. N. L., Fernández, A.,  
903 Almendros-Ibáñez, J., Submitted for publication. Characterization and  
904 testing of solid particles to be used in csp plants: aging and fluidization  
905 tests. *Solar Energy Materials & Solar Cells*.

906 Bellan, S., Kodama, T., Matsubara, K., Gokon, N., Cho, H. S., Inoue, K.,  
907 2019. Thermal performance of a 30 kw fluidized bed reactor for solar  
908 gasification: A cfd-dem study. *Chemical Engineering Journal* 360, 1287–  
909 1300.

910 Benoit, H., López, I. P., Gauthier, D., Sans, J.-L., Flamant, G., 2015. On-  
911 sun demonstration of a 750 c heat transfer fluid for concentrating solar  
912 systems: Dense particle suspension in tube. *Solar Energy* 118, 622–633.

913 Briongos, J., Gómez-Hernández, J., González-Gómez, P., Serrano, D., 2018.  
914 Two-phase heat transfer model of a beam-down gas-solid fluidized bed  
915 solar particle receiver. *Solar Energy* 171, 740–750.

916 Diago, M., Iniesta, A. C., Soum-Glaude, A., Calvet, N., 2018. Character-  
917 ization of desert sand to be used as a high-temperature thermal energy  
918 storage medium in particle solar receiver technology. *Applied energy* 216,  
919 402–413.

920 Díaz-Heras, M., Moya, J., Belmonte, J., Córcoles-Tendero, J., Molina, A.,  
921 Almendros-Ibáñez, J., 2019. Csp on fluidized particles with a beam-down  
922 reflector: Comparative study of different fluidization technologies. *Solar*  
923 *Energy*.

- 924 Elsayed, M. M., Megahed, I., El-Refaee, M., 1988. Experimental testing of  
925 fluidized bed thermal storage. *Solar & wind technology* 5 (1), 15–25.
- 926 Fernández-Torrijos, M., Albrecht, K., Ho, C., 2018. Dynamic modeling of a  
927 particle/supercritical co2 heat exchanger for transient analysis and con-  
928 trol. *Applied energy* 226, 595–606.
- 929 Flamant, G., 1982. Theoretical and experimental study of radiant heat trans-  
930 fer in a solar fluidized-bed receiver. *AIChE Journal* 28 (4), 529–535.
- 931 Flamant, G., Olalde, G., 1983. High temperature solar gas heating com-  
932 parison between packed and fluidized bed receivers. *Solar energy* 31 (5),  
933 463–471.
- 934 García-Triñanes, P., Seville, J., Boissière, B., Ansart, R., Leadbeater, T.,  
935 Parker, D., 2016. Hydrodynamics and particle motion in upward flow-  
936 ing dense particle suspensions: Application in solar receivers. *Chemical*  
937 *Engineering Science* 146, 346–356.
- 938 Geldart, D., 1973. Types of gas fluidization. *Powder technology* 7 (5), 285–  
939 292.
- 940 Glicksman, L., Hyre, M., Woloshun, K., 1993. Simplified scaling relation-  
941 ships for fluidized beds. *Powder Technology* 77 (2), 177–199.
- 942 Glicksman, L. R., 1984. Scaling relationships for fluidized beds. *Chemical*  
943 *engineering science* 39 (9), 1373–1379.
- 944 Grace, J. R., Lim, C. J., 2011. *Spouted and Spout-Fluid Beds*. Cambridge  
945 University Press, Ch. Scaleup, slot–rectangular, and multiple spouting,  
946 pp. 283–296.

947 Guo, Q., Yue, G., Suda, T., Sato, J., 2003. Flow characteristics in a bub-  
948 bling fluidized bed at elevated temperature. *Chemical Engineering and*  
949 *Processing: Process Intensification* 42 (6), 439–447.

950 Ho, C. K., 2016. A review of high-temperature particle receivers for concen-  
951 trating solar power. *Applied Thermal Engineering* 109, 958–969.

952 Ho, C. K., Christian, J. M., Yellowhair, J., Siegel, N., Jeter, S., Golob, M.,  
953 Abdel-Khalik, S. I., Nguyen, C., Al-Ansary, H., 2016. On-sun testing of an  
954 advanced falling particle receiver system. In: *AIP Conference Proceedings*.  
955 Vol. 1734. AIP Publishing LLC, p. 030022.

956 Ho, C. K., Iverson, B. D., 2014. Review of high-temperature central receiver  
957 designs for concentrating solar power. *Renewable and Sustainable Energy*  
958 *Reviews* 29, 835–846.

959 Izquierdo-Barrientos, M., Sobrino, C., Almendros-Ibáñez, J., 2016. Modeling  
960 and experiments of energy storage in a packed bed with pcm. *International*  
961 *Journal of Multiphase Flow* 86, 1–9.

962 Izquierdo-Barrientos, M. A., Sobrino, C., Almendros-Ibáñez, J. A., 2013.  
963 Thermal energy storage in a fluidized bed of pcm. *Chemical engineering*  
964 *journal* 230, 573–583.

965 Izquierdo-Barrientos, M. A., Sobrino, C., Almendros-Ibáñez, J. A., 2015.  
966 Energy storage with pcm in fluidized beds: Modeling and experiments.  
967 *Chemical Engineering Journal* 264, 497–505.

968 Kathuria, D., Saxena, S., 1987. A variable-thickness two-dimensional bed for  
969 investigating gas solid fluidized bed hydrodynamics. *Powder technology*  
970 53 (2), 91–96.

971 Kodama, T., Gokon, N., Matsubara, K., Yoshida, K., Koikari, S., Nagase,  
972 Y., Nakamura, K., 2014. Flux measurement of a new beam-down solar  
973 concentrating system in miyazaki for demonstration of thermochemical  
974 water splitting reactors. *Energy Procedia* 49, 1990–1998.

975 Kunii, D., Levenspiel, O., 2013. *Fluidization engineering*. Elsevier.

976 Kuravi, S., Trahan, J., Goswami, D. Y., Rahman, M. M., Stefanakos, E. K.,  
977 2013. Thermal energy storage technologies and systems for concentrating  
978 solar power plants. *Progress in Energy and Combustion Science* 39 (4),  
979 285–319.

980 Le Gal, A., Grange, B., Tessonnaud, M., Perez, A., Escape, C., Sans, J.,  
981 Flamant, G., 2019. Thermal analysis of fluidized particle flows in a finned  
982 tube solar receiver. *Solar Energy* 191, 19–33.

983 Ma, T., Ren, T., Chen, H., Zhu, Y., Li, S., Ji, G., 2019. Thermal perfor-  
984 mance of a solar high temperature thermochemical reactor powered by a  
985 solar simulator. *Applied Thermal Engineering* 146, 881–888.

986 Ma, Z., Glatzmaier, G., Mehos, M., 2014. Development of solid particle ther-  
987 mal energy storage for concentrating solar power plants that use fluidized  
988 bed technology. *Energy Procedia* 49, 898–907.

989 Ma, Z., Martinek, J., 2017. Fluidized-bed heat transfer modeling for the  
990 development of particle/supercritical-co2 heat exchanger. In: *ASME 2017*  
991 *11th International Conference on Energy Sustainability* collocated with  
992 *the ASME 2017 Power Conference Joint With ICOPE-17, the ASME*  
993 *2017 15th International Conference on Fuel Cell Science, Engineering and*

- 994 Technology, and the ASME 2017 Nuclear Forum. American Society of  
995 Mechanical Engineers Digital Collection.
- 996 Ma, Z., Zhang, R., Sawaged, F., 2017. Design of particle-based thermal  
997 energy storage for a concentrating solar power system. In: ASME 2017  
998 11th International Conference on Energy Sustainability collocated with  
999 the ASME 2017 Power Conference Joint With ICOPE-17, the ASME  
1000 2017 15th International Conference on Fuel Cell Science, Engineering and  
1001 Technology, and the ASME 2017 Nuclear Forum. American Society of  
1002 Mechanical Engineers Digital Collection.
- 1003 Martinek, J., Wendelin, T., Ma, Z., 2018. Predictive performance modeling  
1004 framework for a novel enclosed particle receiver configuration and appli-  
1005 cation for thermochemical energy storage. *Solar Energy* 166, 409–421.
- 1006 Mathur, K., 1974. N., epstein. *Spouted Beds*, Academic Press, New York,  
1007 NY.
- 1008 Matsubara, K., Kazuma, Y., Sakurai, A., Suzuki, S., Soon-Jae, L., Kodama,  
1009 T., Gokon, N., Seok, C. H., Yoshida, K., 2014. High-temperature fluidized  
1010 receiver for concentrated solar radiation by a beam-down reflector system.  
1011 *Energy Procedia* 49, 447–456.
- 1012 Matsubara, K., Sakai, H., Kazuma, Y., Sakurai, A., Kodama, T., Gokon,  
1013 N., Cho, H., Yoshida, K., 2015. Numerical modeling of a two-tower type  
1014 fluidized receiver for high temperature solar concentration by a beam-  
1015 down reflector system. *Energy Procedia* 69, 487–496.
- 1016 Morris, A., Ma, Z., Pannala, S., Hrenya, C., 2016. Simulations of heat trans-

1017 fer to solid particles flowing through an array of heated tubes. Solar En-  
1018 ergy 130, 101–115.

1019 Rüdüsüli, M., Schildhauer, T. J., Biollaz, S. M., van Ommen, J. R., 2012.  
1020 Scale up of bubbling fluidized bed reactors. a review. Powder Technology  
1021 217, 21–38.

1022 Salatino, P., Ammendola, P., Bareschino, P., Chirone, R., Solimene, R.,  
1023 2016. Improving the thermal performance of fluidized beds for concen-  
1024 trated solar power and thermal energy storage. Powder technology 290,  
1025 97–101.

1026 Sánchez-Delgado, S., Almendros-Ibáñez, J. A., García-Hernando, N., San-  
1027 tana, D., 2011. On the minimum fluidization velocity in 2d fluidized beds.  
1028 Powder Technology 207 (1-3), 145–153.

1029 Sánchez-González, A., Rodríguez-Sánchez, M. R., Santana, D., 2017. Aiming  
1030 strategy model based on allowable flux densities for molten salt central  
1031 receivers. Solar Energy 157, 1130–1144.

1032 Sánchez-González, A., Rodríguez-Sánchez, M. R., Santana, D., 2018. Aiming  
1033 factor to flatten the flux distribution on cylindrical receivers. Energy 153,  
1034 113–125.

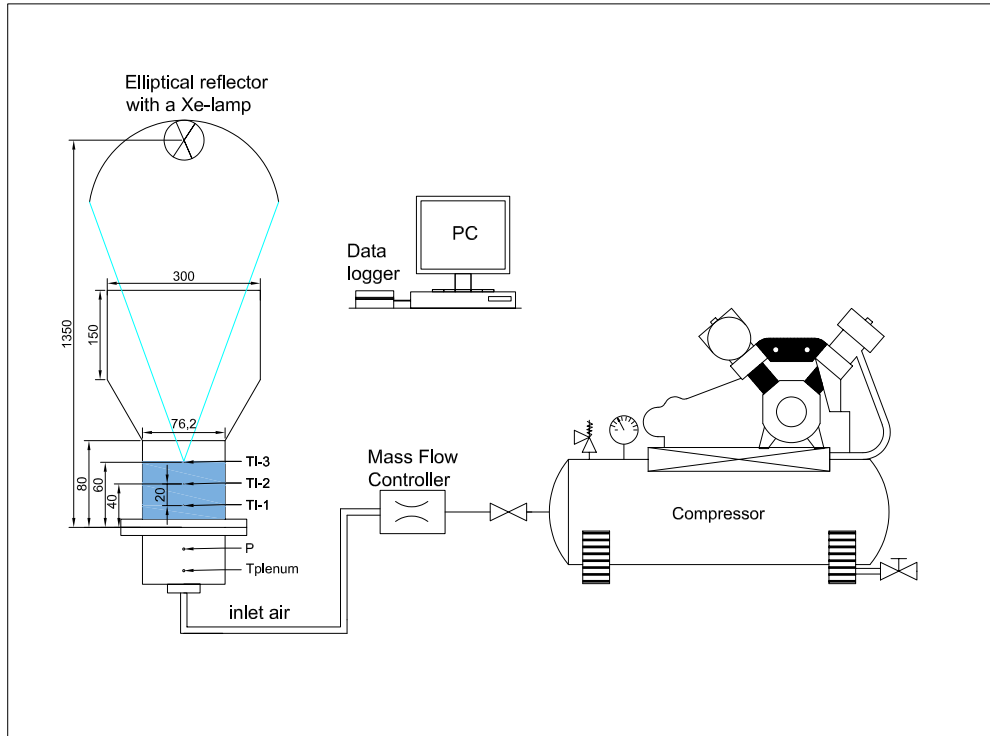
1035 Subramani, H. J., Balaiyya, M. M., Miranda, L. R., 2007. Minimum flu-  
1036 idization velocity at elevated temperatures for geldart’s group-b powders.  
1037 Experimental Thermal and Fluid Science 32 (1), 166–173.

1038 Teske, S., Leung, J., Crespo, L., Bial, M., Dufour, E., Richter, C., Rochon,  
1039 E., 2016. Solar thermal electricity: Global outlook 2016. European Solar  
1040 Thermal Electricity Association.

- 1041 Tregambi, C., Chirone, R., Montagnaro, F., Salatino, P., Solimene, R., 2016.  
1042 Heat transfer in directly irradiated fluidized beds. *Solar Energy* 129, 85–  
1043 100.
- 1044 Vignarooban, K., Xu, X., Arvay, A., Hsu, K., Kannan, A. M., 2015. Heat  
1045 transfer fluids for concentrating solar power systems—a review. *Applied*  
1046 *Energy* 146, 383–396.
- 1047 Xu, C., Li, X., Wang, Z., He, Y., Bai, F., 2013. Effects of solid particle  
1048 properties on the thermal performance of a packed-bed molten-salt ther-  
1049 mocline thermal storage system. *Applied Thermal Engineering* 57 (1-2),  
1050 69–80.
- 1051 Zanganeh, G., Pedretti, A., Zavattoni, S., Barbato, M., Steinfeld, A., 2012.  
1052 Packed-bed thermal storage for concentrated solar power. pilot-scale  
1053 demonstration and industrial-scale design. *Solar Energy* 86 (10), 3084–  
1054 3098.
- 1055 Zhong, W., Chen, X., Zhang, M., 2006. Hydrodynamic characteristics of  
1056 spout-fluid bed: Pressure drop and minimum spouting/spout-fluidizing  
1057 velocity. *Chemical Engineering Journal* 118 (1-2), 37–46.

1058 **List of Figures**

1059	1	Experimental setup used in this work. . . . .	49
1060	2	Schematic diagrams of both fluidization arrangements (bub-	
1061		bling and spouted bed). . . . .	50
1062	3	Simplified schematic diagrams of the two fluidization tech-	
1063		nologies studied: (a) bubbling fluidized bed and (b) spouted	
1064		bed (Díaz-Heras et al., 2019). . . . .	51
1065	4	Radiation maps measured when the radiation power emitted	
1066		by the lamp was 2 and 4 kW. The shaded region represents	
1067		the bed diameter. . . . .	52
1068	5	Minimum fluidization velocities experimentally obtained for	
1069		each of the three materials tested. . . . .	53
1070	6	Temperature profiles as a function of time for the three mate-	
1071		rials considering three excess airflow rates (1.5, 2 and 2.5 $U_{mf}$ ).	
1072		These tests were carried out for a lamp power of 2 $kW_e$ . . . .	54
1073	7	Charging (a) and discharging (b) efficiencies as a function of	
1074		time for the three studied materials, considering three excess	
1075		airflow rates (1.5, 2 and 2.5 $U_{mf}$ ). These tests were carried	
1076		out for a lamp power of 2 $kW_e$ . . . . .	55
1077	8	Temperature profiles as a function of time for the three dif-	
1078		ferent granular materials tested, using different airflow rates	
1079		and lamp powers. . . . .	56
1080	9	Charging efficiencies as a function of time for the three dif-	
1081		ferent granular materials tested, using different airflow rates	
1082		and lamp powers. . . . .	57
1083	10	Temperature evolutions for the three granular materials tested.	
1084		The lamp power was equal to 2 $kW_e$ for both fluidization tech-	
1085		nologies: spouted and bubbling beds. . . . .	58
1086	11	Evolution of the charging (a) and discharging (b) efficiencies	
1087		as a function of time for the three granular materials studied	
1088		when the airflow rates are varied. All tests were carried out	
1089		with a lamp power of 2 $kW_e$ and spouted bed configuration. .	59
1090	12	Ratio between the energy stored in the bed of particles, $E_s$ ,	
1091		and the total energy needed for fluidizing the particles, $W$ ,	
1092		during the charging process in the fluidized bed (a) and in	
1093		the spouted bed(b). . . . .	60

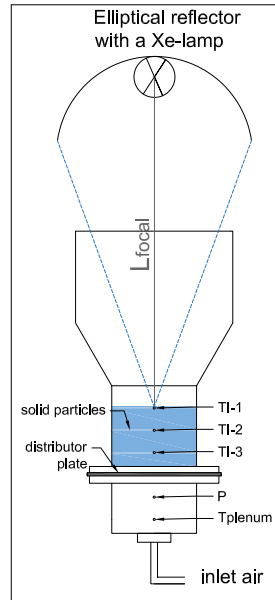


(a) Schematic diagram of the experimental facility. Dimensions in millimeters.

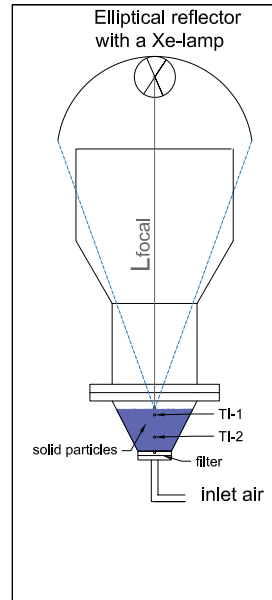


(b) photograph of the bed and beam-down configuration

Figure 1: Experimental setup used in this work.

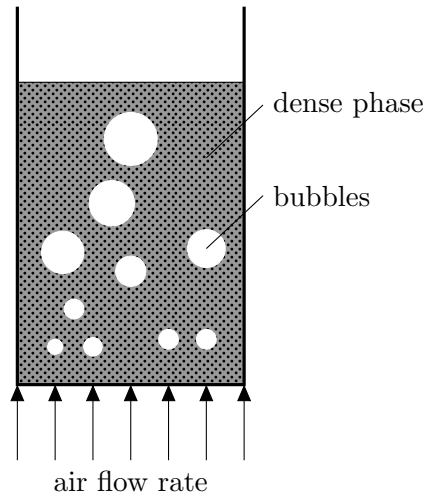


(a) Bubbling bed

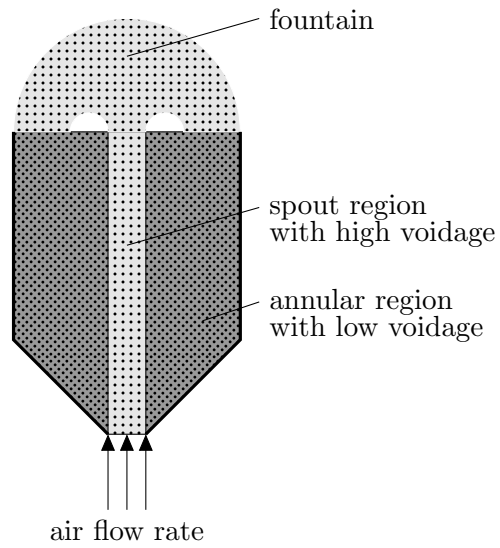


(b) Spouted bed

Figure 2: Schematic diagrams of both fluidization arrangements (bubbling and spouted bed).



(a) bubbling bed



(b) spouted bed

Figure 3: Simplified schematic diagrams of the two fluidization technologies studied: (a) bubbling fluidized bed and (b) spouted bed (Díaz-Heras et al., 2019).

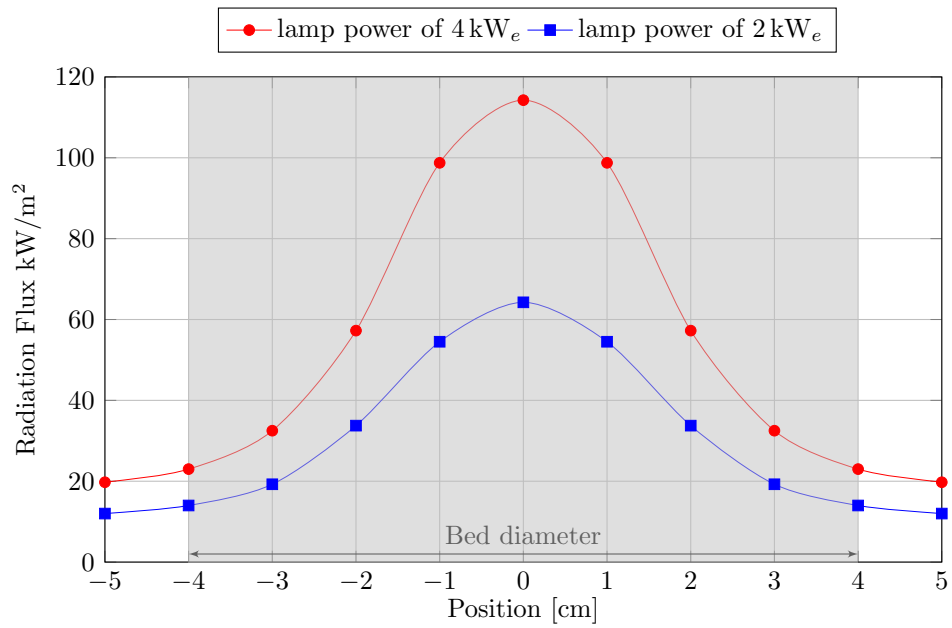


Figure 4: Radiation maps measured when the radiation power emitted by the lamp was 2 and 4 kW. The shaded region represents the bed diameter.

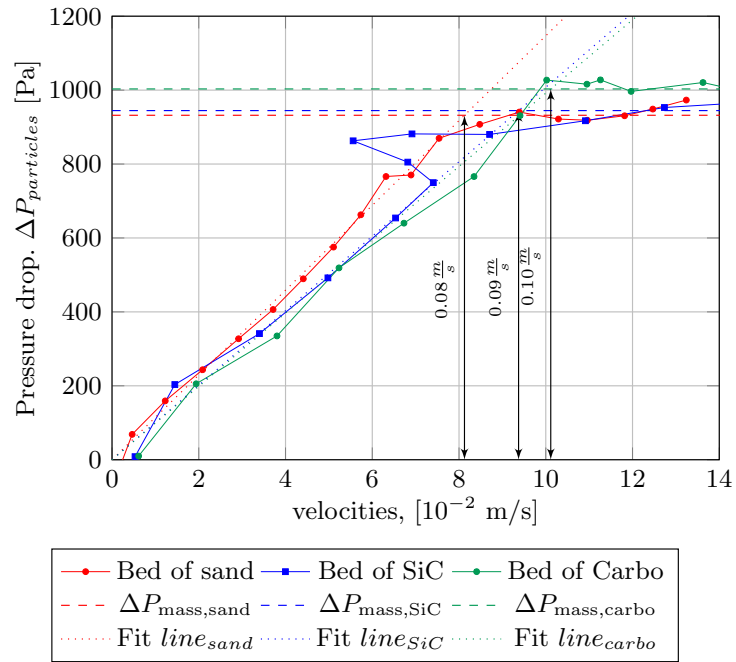


Figure 5: Minimum fluidization velocities experimentally obtained for each of the three materials tested.

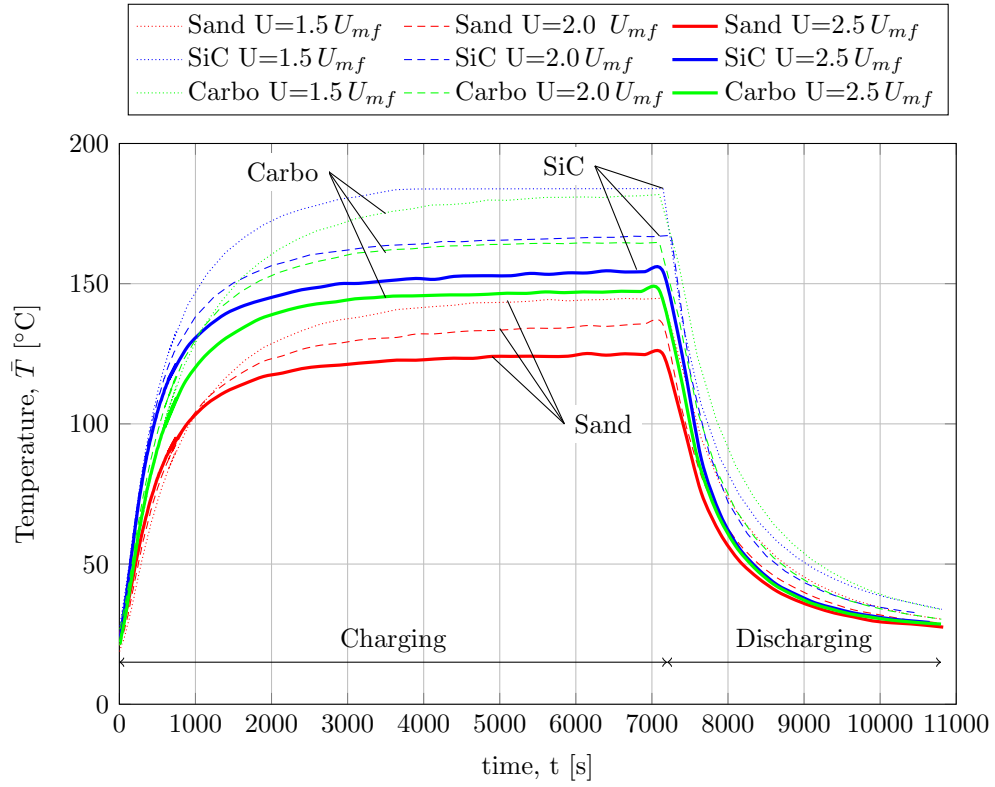
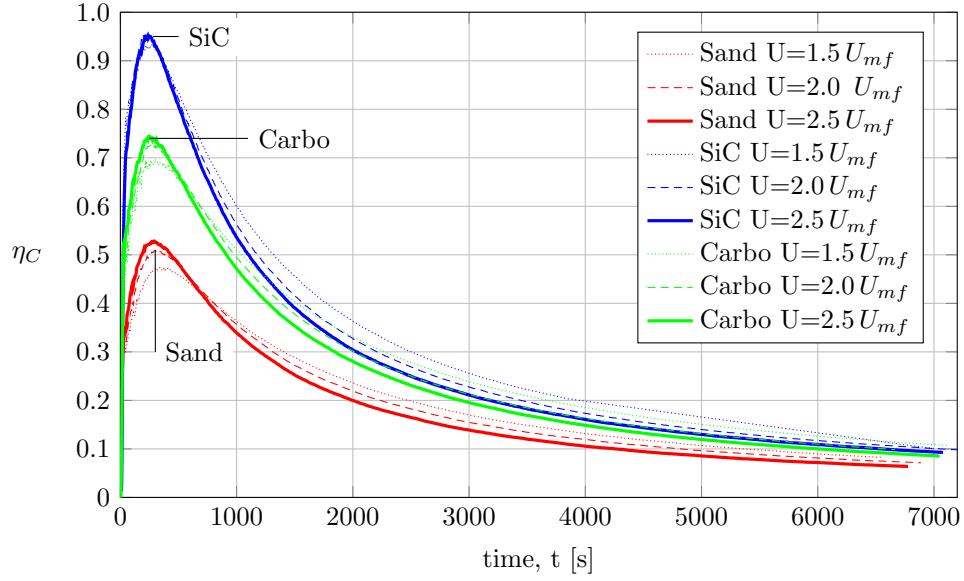
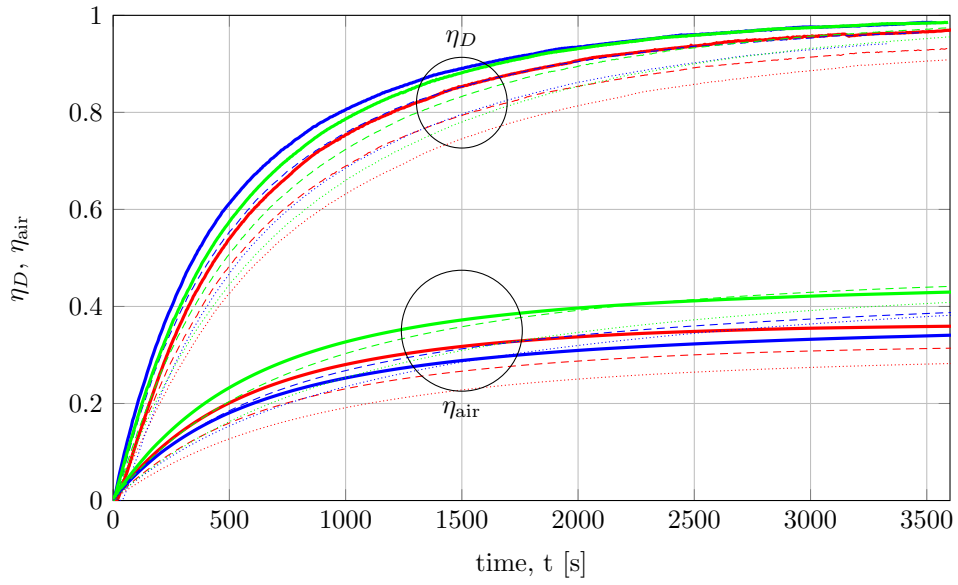


Figure 6: Temperature profiles as a function of time for the three materials considering three excess airflow rates (1.5, 2 and 2.5  $U_{mf}$ ). These tests were carried out for a lamp power of 2  $kW_e$ .

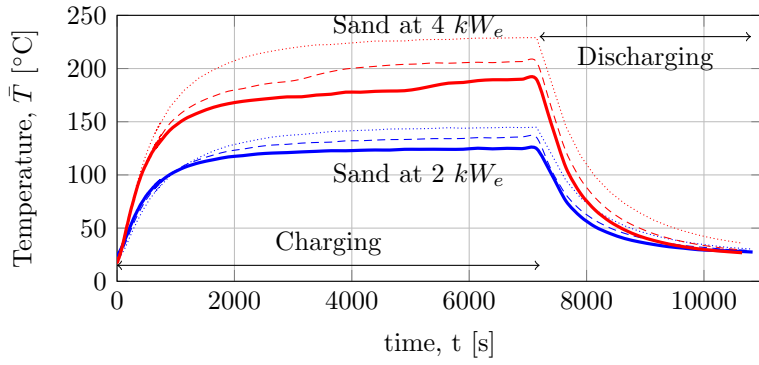


(a) Charging efficiency

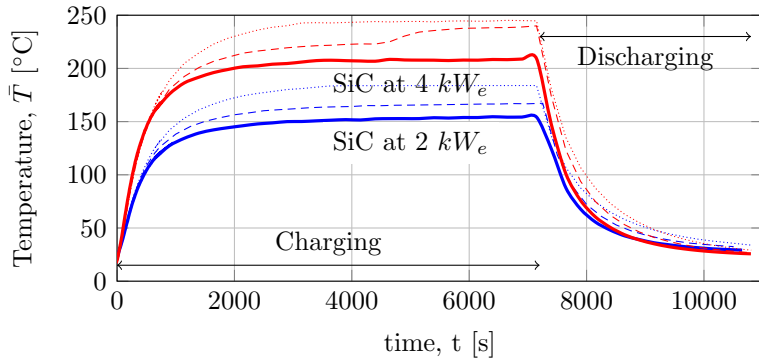


(b) Discharging and air efficiencies

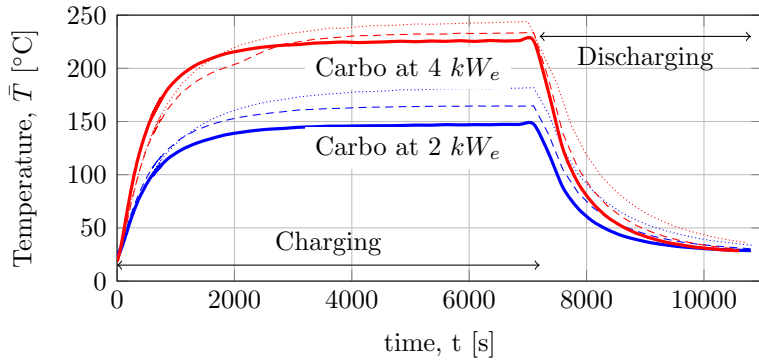
Figure 7: Charging (a) and discharging (b) efficiencies as a function of time for the three studied materials, considering three excess airflow rates (1.5, 2 and  $2.5 U_{mf}$ ). These tests were carried out for a lamp power of  $2 kW_e$ .



(a) Sand



(b) SiC



(c) Carbo

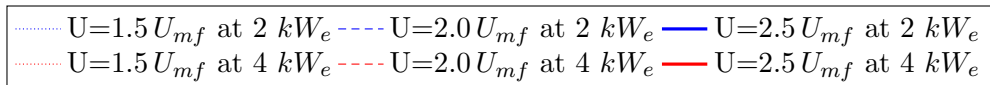
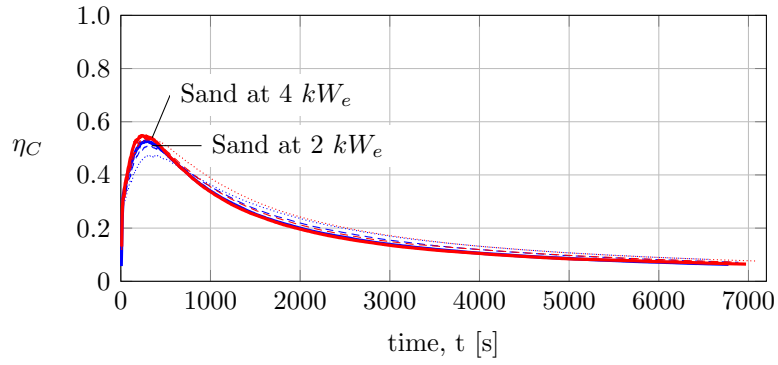
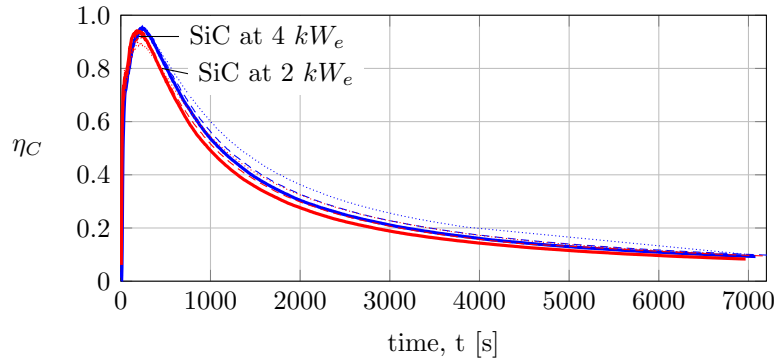


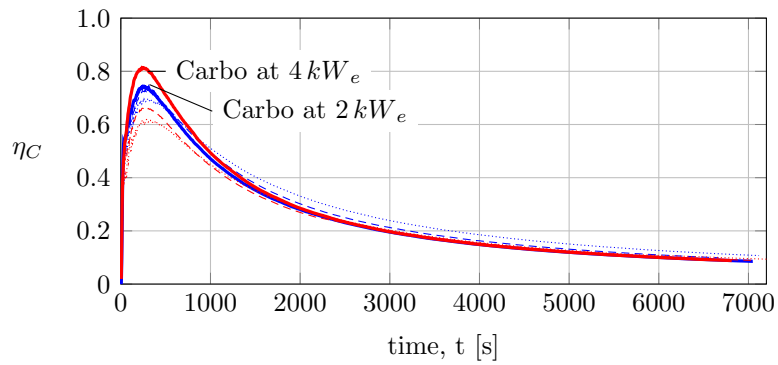
Figure 8: Temperature profiles as a function of time for the three different granular materials tested, using different airflow rates and lamp powers.



(a) Sand



(b) SiC



(c) Carbo

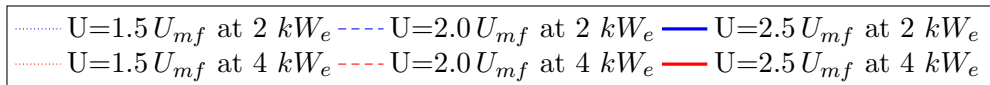
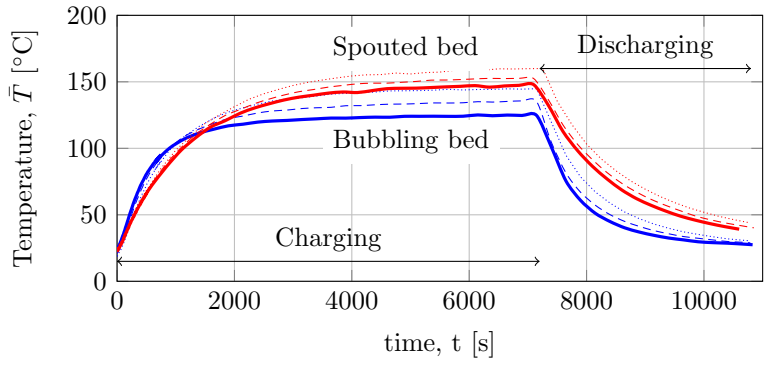
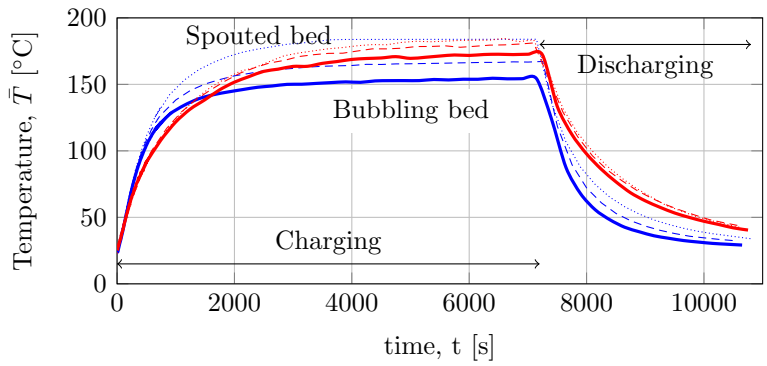


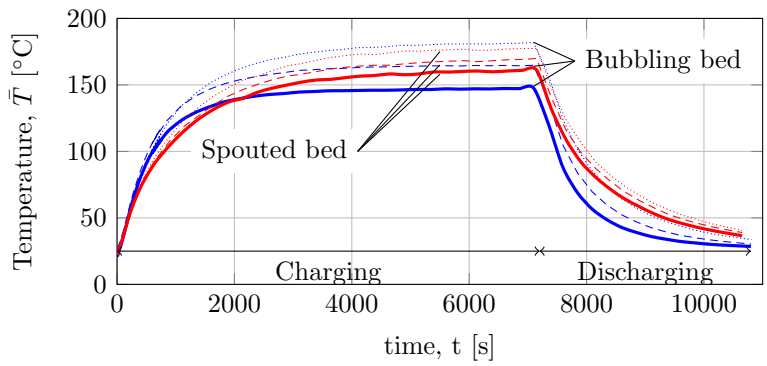
Figure 9: Charging efficiencies as a function of time for the three different granular materials tested, using different airflow rates and lamp powers.



(a) Sand



(b) SiC



(c) Carbo

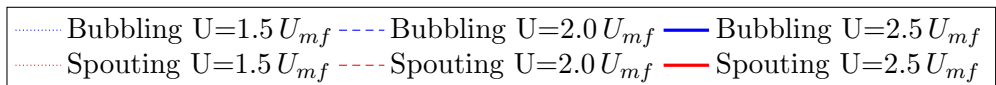
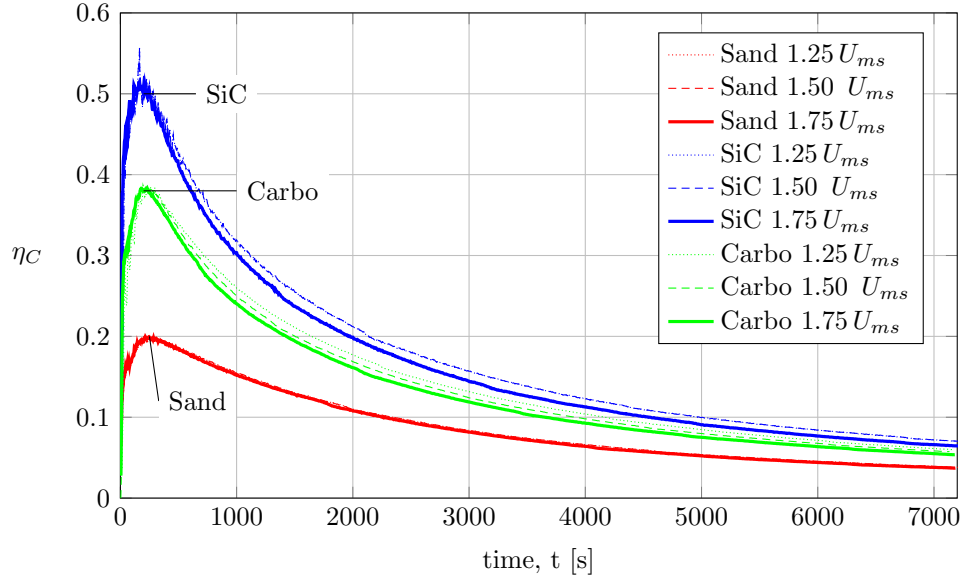
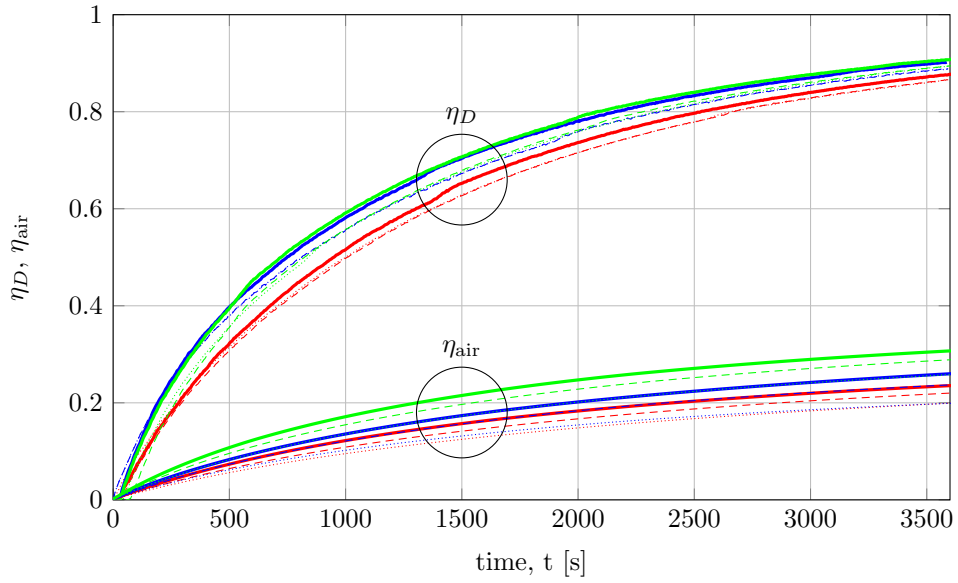


Figure 10: Temperature evolutions for the three granular materials tested. The lamp power was equal to  $2 kW_e$  for both fluidization technologies: spouted and bubbling beds.

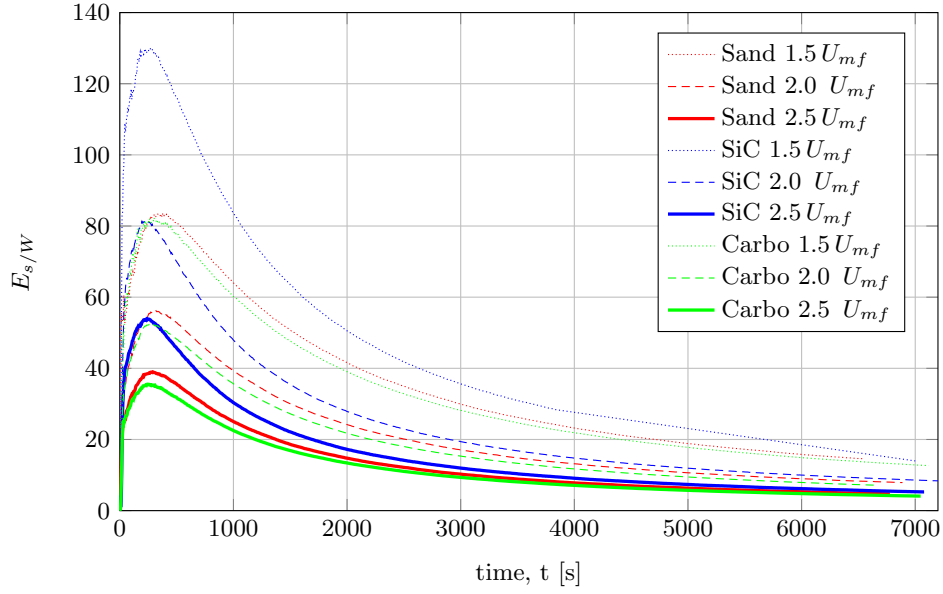


(a) Charging efficiency

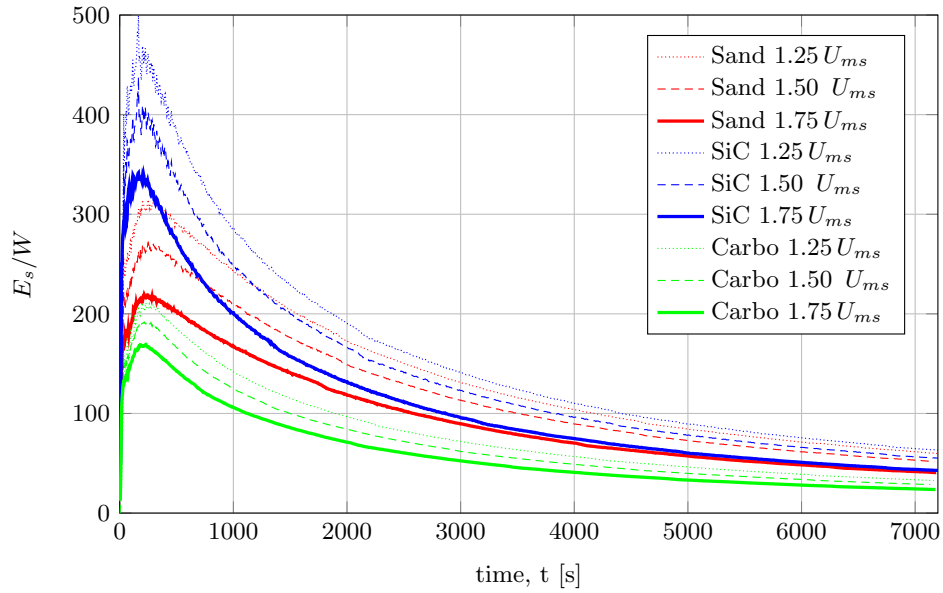


(b) Discharging and air efficiencies

Figure 11: Evolution of the charging (a) and discharging (b) efficiencies as a function of time for the three granular materials studied when the airflow rates are varied. All tests were carried out with a lamp power of  $2 kW_e$  and spouted bed configuration.



(a) Bubbling fluidized bed



(b) Spouted bed

Figure 12: Ratio between the energy stored in the bed of particles,  $E_s$ , and the total energy needed for fluidizing the particles,  $W$ , during the charging process in the fluidized bed (a) and in the spouted bed (b).

1094 **List of Tables**

1095	1	Summary of the properties of the granular materials tested	
1096		in the experiments (Barreneche et al., Submitted for publi-	
1097		cation). Costs have been evaluated according to the price of	
1098		the material when ten tonnes are purchased. . . . .	62
1099	2	Summary of the measurement ranges and uncertainties for	
1100		the measurement instruments used in the experimental tests.	63
1101	3	Summary of the minimum spouting and fluidization velocities	
1102		and airflow rates. . . . .	64
1103	4	Power needed (in Watts) for air pumping in each case. . . .	65
1104	5	Mass of particles used for each fluidization technique and dif-	
1105		ferent material. . . . .	66

	$\rho$ ( $\frac{kg}{m^3}$ )	$c_p$ ( $\frac{kJ}{kg \cdot K}$ )	$d_{90}$ (mm)	<i>Absorptivity</i> (-)	<i>Cost</i> (€/kg)
Sand	2630 ± 40	1.05	0.47	0.49	0.44
SiC	3220 ± 140	1.27	0.41	0.90	2.40
Carbo	3350 ± 210	1.08	0.36	0.95	1.70

Table 1: Summary of the properties of the granular materials tested in the experiments (Barreneche et al., Submitted for publication). Costs have been evaluated according to the price of the material when ten tonnes are purchased.

Measurement instruments	Measuring ranges	Uncertainty
Type-T thermocouples	0-400°C	$\pm 0.2$ °C
Type-A pressure sensor	Plenum: 0-600 mbar Bed: 0-100 mbar	$\pm 3$ mbar $\pm 0.5$ mbar
Mass flow controller	0-200 l/min	$\pm 0.1$ l/min
Radiation sensor	0-3750 kW/m <sup>2</sup>	$\pm 0.25$ kW/m <sup>2</sup>

Table 2: Summary of the measurement ranges and uncertainties for the measurement instruments used in the experimental tests.

	$U_{ms} (\frac{m}{s})$	$U_{mf} (\frac{m}{s})$	$\dot{V}_{ms} (\frac{l}{min})$	$\dot{V}_{mf} (\frac{l}{min})$
Sand	0.42	0.08	8.00	24.51
SiC	0.53	0.09	10.00	28.27
Carbo	0.69	0.10	13.00	30.51

Table 3: Summary of the minimum spouting and fluidization velocities and airflow rates.

	<b>Fluidized bed</b>				<b>Spouted bed</b>			
	$U/U_{mf}$				$U/U_{ms}$			
	<b>1.00</b>	<b>1.50</b>	<b>2.00</b>	<b>2.50</b>	<b>1.00</b>	<b>1.25</b>	<b>1.50</b>	<b>1.75</b>
<b>Sand</b>	0.449	0.798	1.275	1.906	0.052	0.063	0.073	0.090
<b>SiC</b>	0.549	1.010	1.650	2.483	0.095	0.110	0.126	0.149
<b>Carbo</b>	0.639	1.191	1.951	2.944	0.130	0.181	0.198	0.224

Table 4: Power needed (in Watts) for air pumping in each case.

	Sand	SiC	Carbo
$m_B$	558 g	567 g	661 g
$m_S$	200 g	245 g	255 g

Table 5: Mass of particles used for each fluidization technique and different material.